*J. Fluid Mech.* (2001), *vol.* 433, *pp.* 161–192. Printed in the United Kingdom



# Rip current instabilities

By MERRICK C. HALLER† AND R. A. DALRYMPLE

Center for Applied Coastal Research, University of Delaware, Newark, DE 19716, USA

(Received 5 January 2000 and in revised form 9 August 2000)

A laboratory experiment involving rip currents generated on a barred beach with periodic rip channels indicates that rip currents contain energetic low-frequency oscillations in the presence of steady wave forcing. An analytic model for the time-averaged flow in a rip current is presented and its linear stability characteristics are investigated to evaluate whether the rip current oscillations can be explained by a jet instability mechanism. The instability model considers spatially growing disturbances in an offshore directed, shallow water jet. The effects of variable cross-shore bathymetry, non-parallel flow, turbulent mixing, and bottom friction are included in the model. Model results show that rip currents are highly unstable and the linear stability model can predict the scales of the observed unsteady motions.

## 1. Introduction

Rip currents are narrow, seaward-directed currents that extend from the inner surf zone out through the line of breaking waves. In general, rip currents return the water carried landward by waves and, under certain conditions of nearshore slope and wave activity, rip currents are the primary agent for the seaward transport of water and sediment. Rip currents are usually narrow (extending 10–20 m in the longshore direction) and generally span the entire water column; however, offshore of the region of breaking waves they tend to be confined near the surface (Shepard, Emery & La Fond 1941).

In general, rip currents arise from longshore variations in the incident wind wave forcing. For example, periodic longshore variations in the incident wave field can drive coherent nearshore circulation cells. These cells exhibit broad regions of shoreward flow separated by narrow regions of offshore directed flow. If these narrow regions of offshore flow are sufficiently strong, they will appear as rip currents. The necessary longshore variability in wave height can be imposed by boundary effects (e.g. non-planar beaches or groin fields) or by a superposition of wavetrains (e.g. Bowen 1969; Dalrymple 1975). Additionally, rip current circulations may arise as an instability to the nearshore vorticity balance (Iwata 1976; Dalrymple & Lozano 1978). In these models, rip current circulations derive their energy from the incident waves through a feedback mechanism such that an initial wave height variation causes an incipient rip to form which modifies the incident wave field and, in turn, feeds more energy into the circulation system.

Field observations of rip currents indicate that rip currents can exhibit long period oscillations (e.g. Sonu 1972; Bowman *et al.* 1988; and many others). These oscillations have generally been attributed to long period modulations in incoming wave heights

† Present address: Cooperative Institute for Limnology and Ecosystems Research, University of Michigan, 2200 Bonisteel Blvd, Ann Arbor, MI 48109-2099, USA.

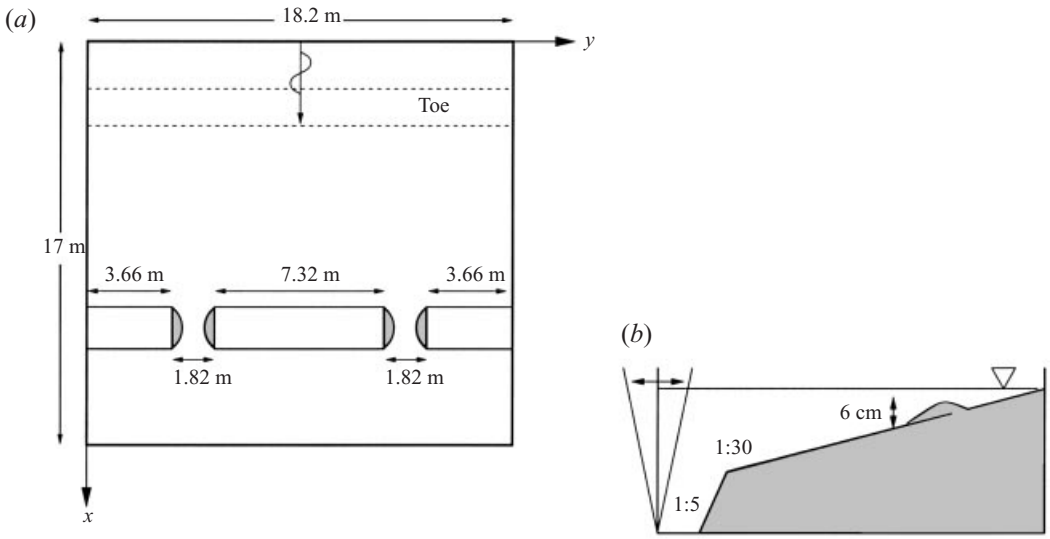


FIGURE 1. (*a*) Plan view and (*b*) cross-section of the experimental basin.

(wave grouping) or to the presence of low-frequency wave motions (surf beat). Recently, it has also been suggested that these oscillations might arise from an instability of the longshore current (Smith & Largier 1995). However, a mechanism for unsteady rip currents that has not yet been addressed is an instability of the rip current flow itself. Rip currents are analogous to plane jets, since they are generally long and narrow and flow offshore into relatively quiescent waters. Hydrodynamic jets have long been known to exhibit instabilities (e.g. Schlichting 1933; Bickley 1939), and the work herein is based on this extensive body of hydrodynamic stability theory.

In § 2, we will give a brief description of the experimental facility, the test conditions, and the experimental results that demonstrate the existence of low-frequency rip current motions. In § 3, we derive the governing vorticity equations for the time-averaged rip current flow and for rip current instabilities. We will formulate a set of self-similar solutions for the time-averaged rip current flow, which include viscous and non-parallel effects. Next, we will analyse the stability characteristics of rip currents and the influence of turbulent mixing, bottom friction, and bottom slope on the instabilities. Also, we will compare both the time-averaged and the instability model results with the measured data. The model for the time-averaged rip current flow is shown to compare favourably with the measured mean rip velocities and, in addition, the predicted time and spatial scales of the instabilities compare well with the experimentally measured values. This is followed by a summary in § 4.

## 2. Laboratory measurements of unsteady rip currents

### 2.1. *Experimental set-up*

The laboratory experiments were performed in the directional wave basin located in the Ocean Engineering Laboratory at the University of Delaware. A plan view of the wave basin is shown in figure 1. Figure 1(*a*) also shows the coordinate axes, the origin is located in one corner where the wavemaker and one sidewall meet. The internal dimensions of the wave basin are approximately 17.2 m in length and 18.2 m in width, and the wavemaker consists of 34 paddles of flap-type. The beach consists of a steep

| Test | $H$ (cm) | $T$ (s) | $h_c$ (cm) | $x_{swl}$ (m) |
|---|---|---|---|---|
| B | 4.41 | 1.0 | 4.73 | 14.9 |
| C | 4.94 | 1.0 | 2.67 | 14.3 |
| D | 7.56 | 1.0 | 2.67 | 14.3 |
| E | 3.68 | 0.8 | 2.67 | 14.3 |
| G | 6.79 | 1.0 | 6.72 | 15.4 |

TABLE 1. Table of experimental conditions, mean wave height ($H$) measured near offshore edge of centre bar ($x = 10.92$ m, $y = 9.23$ m), wave period ($T$), average water depth at the bar crest ($h_c$), and cross-shore location of the still water line ($x_{swl}$).

(1 : 5) toe located between 1.5 m and 3 m from the wavemaker with a milder (1 : 30) sloping section extending from the toe to the opposite wall of the basin. Three 'sand bar' sections were constructed in the shape of a generalized bar profile from sheets of high-density polyethylene. The completed bar system consisted of three sections: one main section spanning approximately 7.32 m longshore and two half-sections approximately 3.66 m (longshore) each. In order to ensure that the sidewalls were located along lines of symmetry, the longest section was centred in the middle of the tank and the two half-sections were placed against the sidewalls. This left two gaps of approximately 1.82 m width, located at $\frac{1}{4}$ and $\frac{3}{4}$ of the basin width, that served as rip channels. The edges of the bars on each side of the gaps were rounded off with cement in order to limit wave reflections from the channel sides. The seaward edges of the bar sections were located at approximately $x = 11.1$ m with the bar crest at $x = 12$ m, and their shoreward edges at $x = 12.3$ m. This configuration caused the ratio of rip current spacing to surf zone width to range between 2.7 and 4.0 during the experiments (depending on the still water level). In the field, this ratio has been found to vary between 1.5 and 8 (Huntley & Short 1992).

The waves were generated using linear wave theory and all of the tests discussed herein consist of monochromatic normally incident waves. The experimental conditions such as wave height ($H$), wave period ($T$), water depth at the bar crest ($h_c$), and shoreline location ($x_{swl}$), are given in table 1.

The measuring instruments consisted of ten capacitance wave gauges and three acoustic Doppler velocimeters (ADVs). For most experimental runs, data were sampled at 10 Hz by each sensor, the start of data acquisition coincided with the onset of wave generation, and 16 384 data points were collected (some runs were longer). The velocity measurements during test B spanned the widest range of spatial locations encompassing both sides of one rip channel and much of the area shoreward of the bars ($8.9\text{ m} < x < 13.9\text{ m}$, $3.2\text{ m} < y < 16.2\text{ m}$). During the remaining tests, the velocity measurements were concentrated near one rip current ($13\text{ m} < y < 14.2\text{ m}$) and in the feeder current shoreward of the central bar ($12.2\text{ m} < x < 13.4\text{ m}$, $9.2\text{ m} < y < 11.8\text{ m}$). The experimental procedures are discussed in detail in Haller, Dalrymple & Svendsen (2000).

### 2.2. *Experimental results*

The experimental bathymetry was designed to set up a nearshore circulation system consisting of two pairs of counter-rotating circulation cells that drive rip currents through each rip channel. These cells are forced by the longshore variation in wave breaking that is intimately related to the presence of the bars. The strong wave breaking where the water is shallow over the bar crests induces a relatively higher

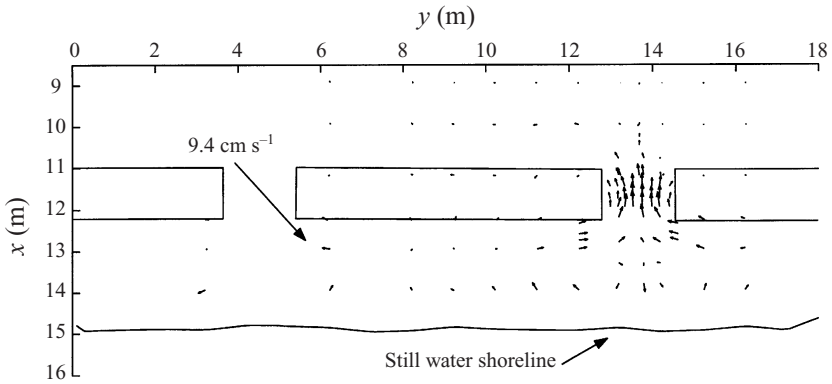


FIGURE 2. Measured mean current vectors for test B. Means computed by averaging the last 15 360 points ($102.4\,\mathrm{s} < t \leqslant 1638.4\,\mathrm{s}$) of each time series.

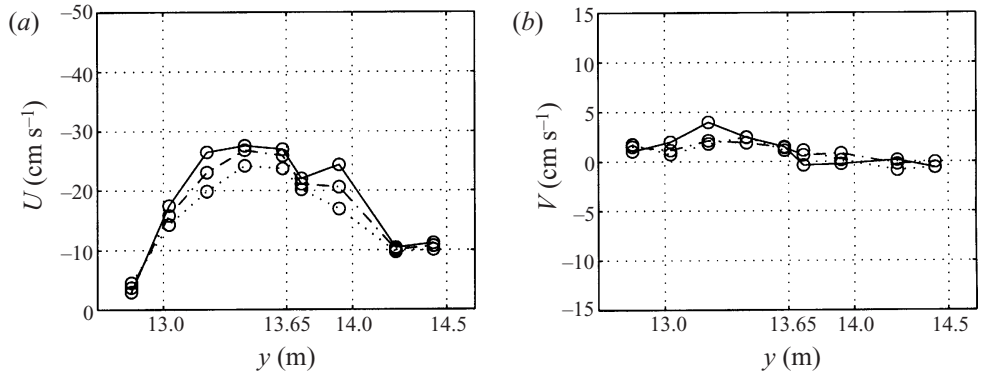


FIGURE 3. Mean velocities measured in the rip channel: —, $x = 11.63\,\mathrm{m}$; ---, $x = 11.43\,\mathrm{m}$; $\cdots$, $x = 11.23\,\mathrm{m}$; for test C, (*a*) cross-shore velocities, (*b*) longshore velocities.

wave set-up shoreward of the bars. In the rip channels, there is a relatively lower wave set-up owing to the very mild wave breaking. The masses of water piled up behind the bar flows alongshore towards the channels where the flows converge and turn offshore in the rips. This nearshore circulation system can be seen clearly in figure 2 (for a more thorough discussion of the measured circulation see Haller & Dalrymple 1999).

The instantaneous cross-shore velocities in the laboratory rip currents were as large as 60–70 $\mathrm{cm\,s^{-1}}$ depending on the incident wave conditions and still water depth. Examples of the measured mean cross-shore ($U$) and longshore ($V$) velocity profiles are shown in figure 3. The profiles indicate that there is a significant amount of shear in the cross-shore velocity profile, which suggests the flow may be unstable. Also, it is evident that the longshore component of the flow is rather small.

Time series of cross- and longshore velocities measured in the narrow, jet-like region (rip neck) of the rip current during test C are shown in figure 4. The time series show distinct low-frequency oscillations throughout most of the recording period. However, the oscillations are more visually apparent in the longshore component of the flow. This is due to the strong wave orbital velocities in the cross-shore signal of the normally incident waves.

In order to determine the relative amplitudes of the low-frequency oscillations in the

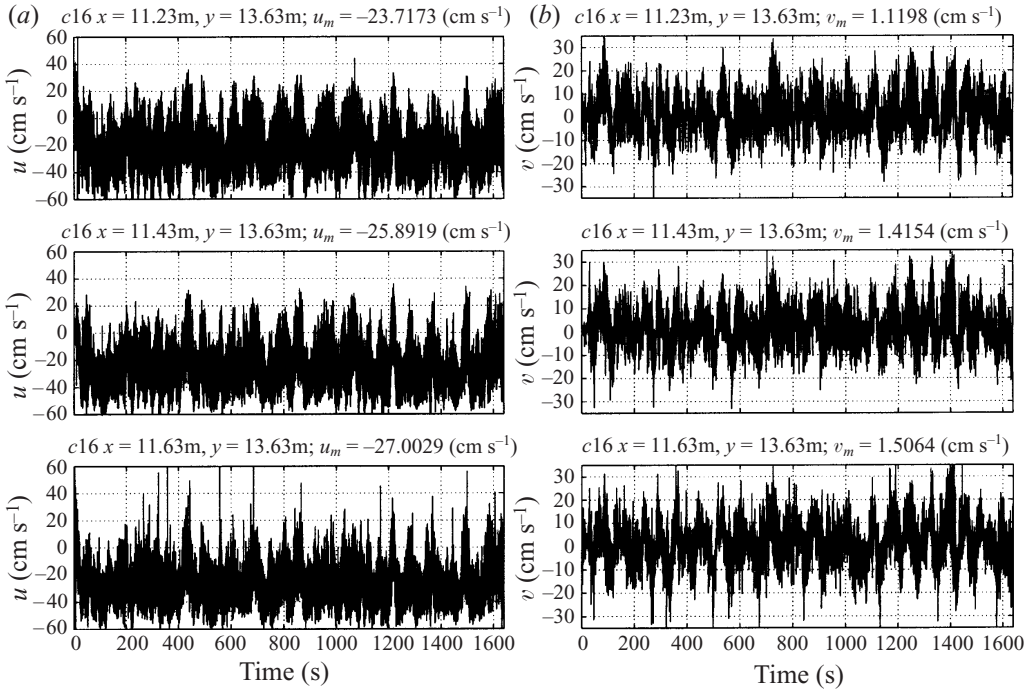


FIGURE 4. Time series of (*a*) cross-shore velocity (*u*), (*b*) longshore velocity (*v*) measured near the centre of the rip channel (test C, run 16; $x = 11.23$, 11.43, 11.63 m; $y = 13.63$ m).

| Test | B | C | D | E | G |
|---|---|---|---|---|---|
| $\sigma_u$ | 3.7 | 7.0 | 7.5 | 6.0 | 6.2 |
| $\sigma_v$ | 8.5 | 4.9 | 3.4 | 5.6 | 5.1 |
| $U_{max}$ | −19.7 | −27.6 | −40.8 | −21.6 | −21.8 |
| $x$ | 11.94 | 11.63 | 11.43 | 11.93 | 11.93 |
| $y$ | 13.53 | 13.43 | 14.24 | 14.24 | 13.63 |

TABLE 2. Table of standard deviations of lowpass filtered cross-shore, $\sigma_u$, and longshore, $\sigma_v$, velocities (cm s$^{-1}$) measured in the rip neck. $U_{max}$ is the maximum mean offshore current (cm s$^{-1}$), $x, y$ are the measuring locations (m).

rip neck, the velocity data from each test were lowpass filtered ($0 < f < 0.033$ Hz) to remove the incident wave signal and any motions due to basin seiching (see Appendix A for seiching analysis). The standard deviations ($\sigma_u, \sigma_v$) of the filtered records are shown in table 2 along with the mean of the unfiltered cross-shore velocity record. The particular data record chosen for each test corresponds to the record from the location of the maximum measured mean offshore rip velocity. It is apparent from this data that $\sigma_u$ and $\sigma_v$ are of comparable amplitude and are a significant percentage of the mean velocity. The data indicate some variability in the magnitudes of $\sigma_u$ and $\sigma_v$. This is mostly due to variability in the location of the measured maximum ($U_{max}$). Additional variability is likely owing to variability in the mean rip current direction, which was not always directly offshore. However, the variabilty of the total low-frequency current vector ($\sigma_{|\boldsymbol{u}|}$) at the rip maximum was much smaller ($\pm 1.3$ cm s$^{-1}$).

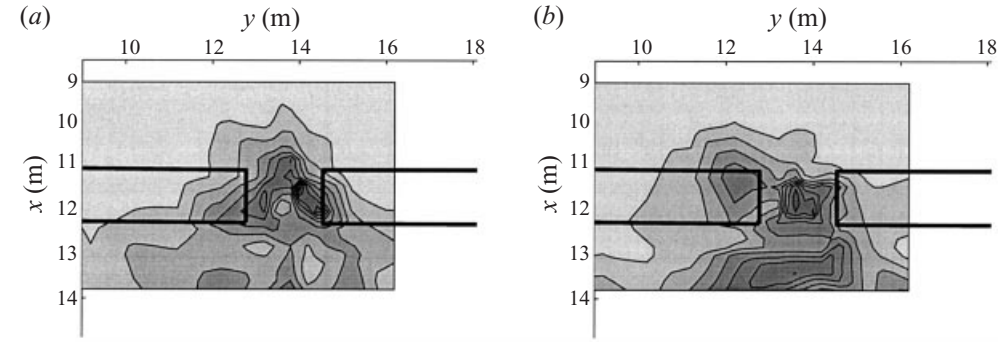


FIGURE 5. Contours of low-frequency ($f \leqslant 0.033$ Hz) variance for test B, (*a*) cross-shore variance ($\sigma_u^2$), maximum contour 74.1 cm$^2$ s$^{-2}$ (*b*) longshore variance ($\sigma_v^2$), maximum contour 82.3 cm$^2$ s$^{-2}$. Contour interval is 8.23 cm$^2$ s$^{-2}$.

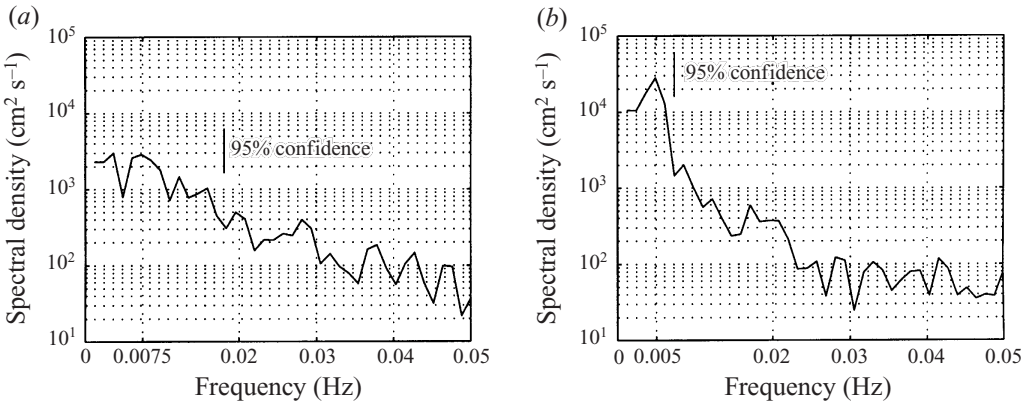


FIGURE 6. Average energy spectrum of (*a*) cross-shore velocities and (*b*) longshore velocities measured near the rip neck (test B, run 33; 275.2 s $< t <$ 2732.7 s; $x = 11.44$ m, 11.74 m, 11.94 m; $y = 13.53$ m), $\Delta f = 0.0012$, d.o.f. = 18.

It is also important to note that these low-frequency current oscillations are localized near the neck. Figure 5 shows the distribution of low-frequency variance ($\sigma_u^2, \sigma_v^2$) throughout the circulation system measured during test B. The contours clearly show a concentration of both $u$ and $v$ variance along the rip axis, especially in the gap between the bars. Since the variance is localized in the location of the rip neck and the frequencies of the motions are much lower than predicted seiching modes (see Appendix A), it is unlikely that basin resonances are a source for these motions. The contours shown in figure 5 also show that the low-frequency variances are much smaller at the basin centre ($y = 9.1$ m) and decay towards zero near the sidewall ($y = 18.2$ m). This suggests that the two rip currents were behaving independently and that the influence of the basin sidewalls on the low-frequency motions should be limited.

Spectral analysis of the velocity records measured along the rip current axis allows us to estimate the specific timescales of these oscillations. Since these motions have such long timescales, the longer time series were used when available. The cross- and longshore velocity spectra from each test along with the 95% confidence intervals and degrees of freedom (d.o.f.) are shown in figures 6–10. Figure 6(*b*) suggests a dominant

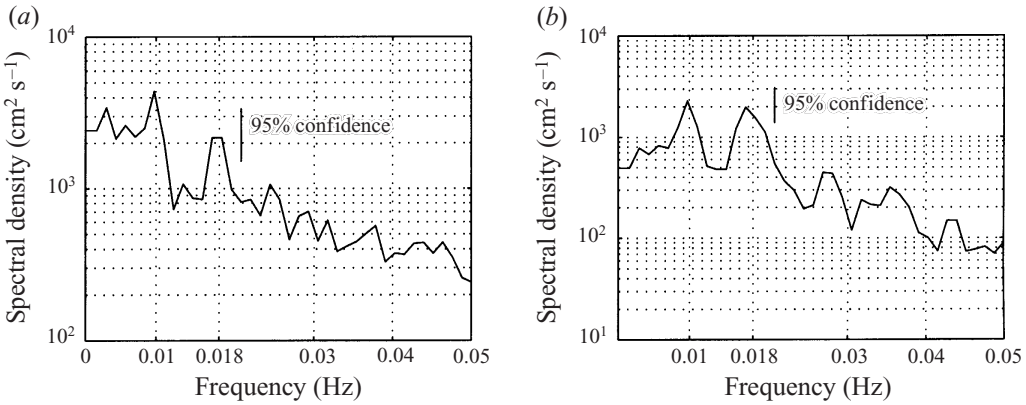


FIGURE 7. Averaged energy spectra of (*a*) cross-shore velocities and (*b*) longshore velocities from extra long time series measured at $x = 11.43$ m, 11.63 m, 11.94 m, $y = 13.63$ m (test C, run 34; $0\,\mathrm{s} < t < 6553.6\,\mathrm{s}$), $\Delta f = 0.0012$ Hz, d.o.f. = 48.

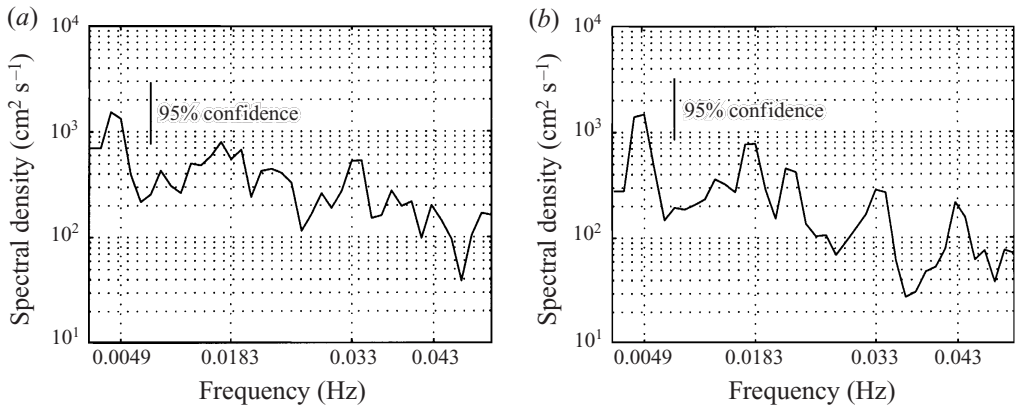


FIGURE 8. Averaged energy spectra of (*a*) cross-shore velocities and (*b*) longshore velocities measured at $x = 11.43$ m, 11.63 m, 11.93 m, $y = 13.03$ m, 13.63 m, 14.24 m (test D, runs D1–3; $819.2\,\mathrm{s} < t < 1638.4\,\mathrm{s}$), $\Delta f = 0.0012$ Hz, d.o.f. = 18.

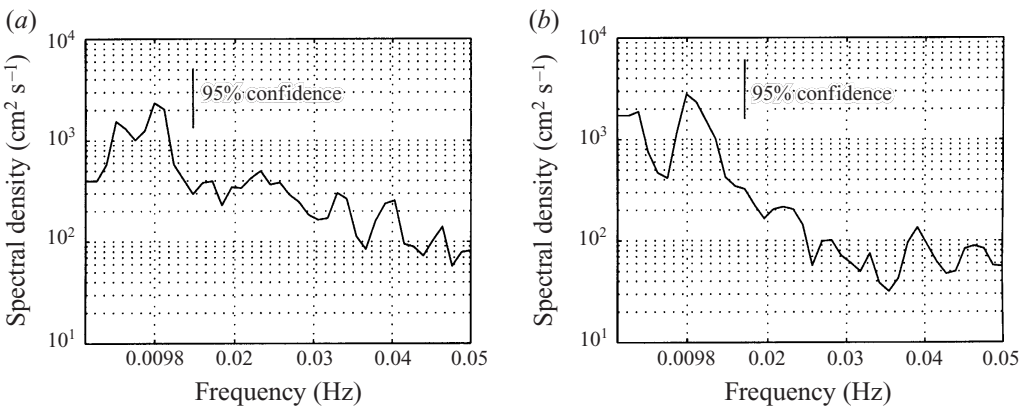


FIGURE 9. Averaged energy spectra of (*a*) cross-shore velocities and (*b*) longshore velocities measured at $x = 11.43$ m, 11.63 m, 11.93 m, $y = 13.03$ m, 13.63 m, 14.24 m (test E, runs E1–3; $819.2\,\mathrm{s} < t < 1638.4\,\mathrm{s}$), $\Delta f = 0.0012$ Hz, d.o.f. = 18.

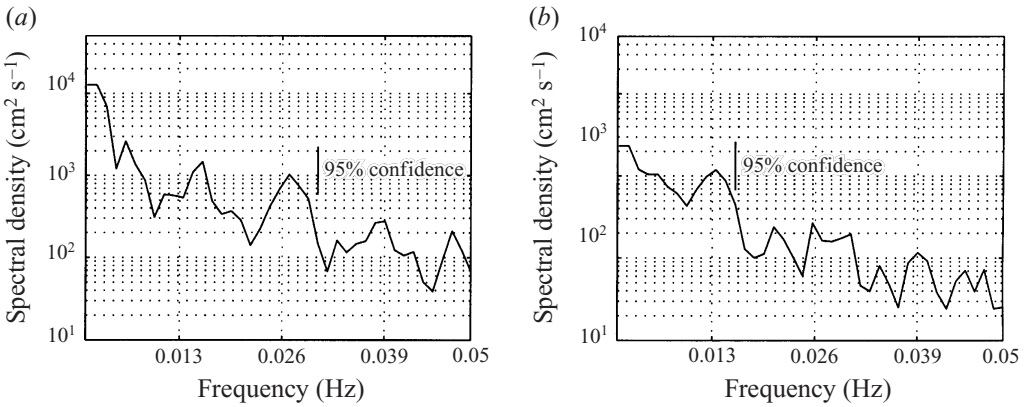


FIGURE 10. Averaged energy spectra of (*a*) cross-shore velocities and (*b*) longshore velocities measured at $x = 11.43$ m, 11.63 m, 11.93 m, $y = 13.03$ m, 13.63 m, 14.24 m (test G, runs G1–3; 819.2 s $< t <$ 1638.4 s), $\Delta f = 0.0012$ Hz, d.o.f. = 18.

low-frequency mode of approximately 0.005 Hz for this test, which is an unusually large timescale for laboratory scale systems.

Figure 7 shows the spectra from test C, which has the most degrees of freedom owing to its long length. The spectra clearly show energy peaks near 0.018 Hz in both the cross-shore and longshore velocities. The spectra also indicate a lower-frequency peak near 0.01 Hz. The $v$ spectrum also shows higher-frequency peaks near 0.028 and 0.036 Hz. The presence of these peaks suggests that the motions at the two low-frequency peaks are interacting nonlinearly, since the higher-frequency peaks centred at 0.028 Hz and 0.036 Hz are a sum frequency (0.01 + 0.018 Hz) and a harmonic (0.018 + 0.018 Hz).

The averaged rip current spectra for tests D, E, and G (figures 8–10) use the data from the three runs during each test when the ADVs were in the rip channel (1 run contains 3 records), and therefore include more spatial averaging. Figure 8 and, to a lesser extent, figure 10 again suggest that specific modes are interacting nonlinearly. Figure 8(*b*) shows numerous distinct peaks in the longshore velocity spectrum, while in the cross-shore spectrum the peaks are less distinct. The dominant longshore velocity peaks are at $f_1 = 0.0049$ Hz, $f_2 = 0.0183$ Hz, and $f_3 = 0.033$ Hz. Here, again, there appear to be interaction peaks at 0.013 Hz ($f_2 - f_1$) and 0.023 Hz ($f_2 + f_1$). However, it is difficult to determine more definitively whether these low-frequency peaks are interacting nonlinearly. The multiple peaks might also indicate the presence of multiple independent linear modes.

Test E had similar wave height and rip current strength to test B. Likewise, the spectra from test E (figure 9) do not show numerous energetic peaks above 0.01 Hz. Instead, test E shows very low-frequency peaks near 0.005 Hz and 0.01 Hz in both cross-shore and longshore velocity spectra. The spectral peaks for test G (figure 10) appear somewhat less distinct than those in tests C and D, however, the presence of energies near 0.013, 0.026, and 0.039 Hz again suggest that harmonics are present.

In order to gain an estimate of the lengthscales of the disturbances measured during the experiments, cross-spectra of longshore velocities were computed from runs when the ADVs were positioned in a cross-shore array located in the rip channel. Since there were only three ADVs in operation during the experiments, and therefore only three sensor lags to compute cross-spectra, it was difficult to obtain statistically meaningful

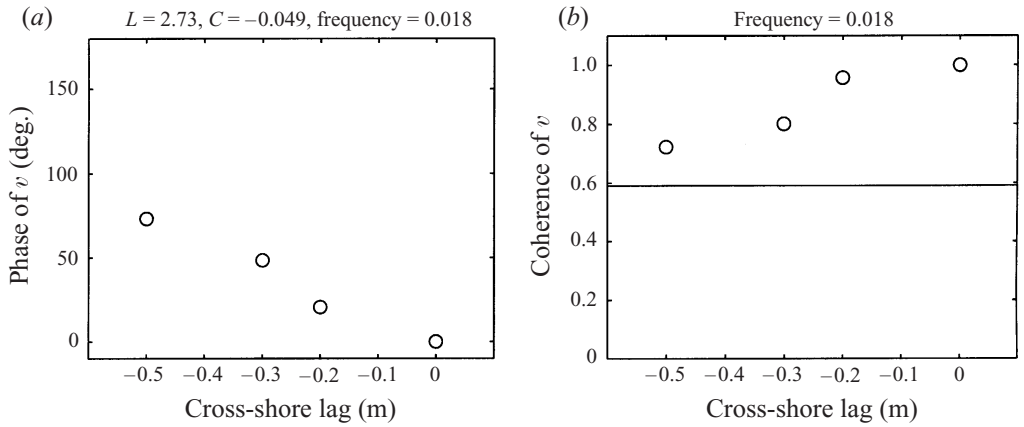


FIGURE 11. (*a*) Phase *vs.* cross-shore sensor separation, (*b*) coherence *vs.* cross-shore sensor separation for test C, run 34, $\Delta f = 0.0012$ Hz, d.o.f. = 16. Solid line indicates 95% confidence level. Phase speed ($C$) defined as $L \times freq$, negative values indicate offshore propagation.

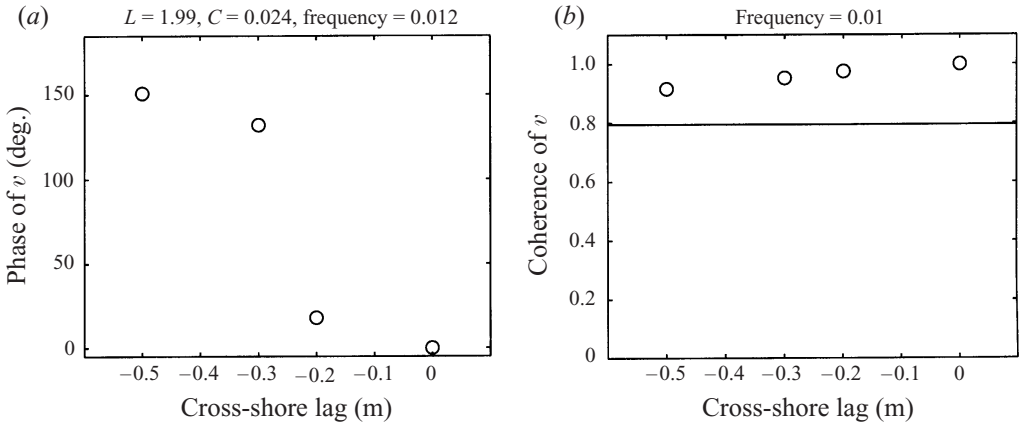


FIGURE 12. (*a*) Phase *vs.* cross-shore sensor separation, (*b*) coherence *vs.* cross-shore sensor separation for test G, run 3, $\Delta f = 0.0024$ Hz, d.o.f. = 8. Solid line indicates 95% confidence level. Phase speed ($C$) defined as $L \times freq$, negative values indicate offshore propagation.

estimates of the disturbance wavelengths. However, figures 11 and 12 show the phase and coherence as a function of cross-shore lag for two frequency bins during tests C and G. Using the average phase variation as a function of distance, we can estimate the wavelength ($L$) of the coherent motions at these frequencies. The experimental estimates of the disturbance lengthscales are shown to be $L = 2.7$ m at $f = 0.018$ Hz test C, and $L = 2$ m at $f = 0.012$ Hz test G. These scales will be shown to compare favourably with the model results given in § 3.

## 3. Rip current modelling

In this section we will concentrate on the modelling of a rip current in isolation. The results shown in § 2.2 indicate that we may neglect the effects of the sidewalls and of rip current coupling. Therefore, we will consider a single rip current initialized at one boundary of a semi-infinite horizontal domain with a finite water depth.

### 3.1. *Governing equations*

In order to model the rip current, we begin with the wave- and depth-averaged equations of motion (after Mei 1989),

$$\hat{u}^*_t + \hat{u}^*\hat{u}^*_x + \hat{v}^*\hat{u}^*_y = -g\hat{\eta}^*_x + \hat{R}^*_x + \hat{M}^*_x + \hat{\mathscr{T}}^*_x, \tag{3.1}$$

$$\hat{v}^*_t + \hat{u}^*\hat{v}^*_x + \hat{v}^*\hat{v}^*_y = -g\hat{\eta}^*_y + \hat{R}^*_y + \hat{M}^*_y + \hat{\mathscr{T}}^*_y, \tag{3.2}$$

$$(\hat{u}^*\hat{h}^*)_x + (\hat{v}^*\hat{h}^*)_y = -\hat{\eta}^*_t, \tag{3.3}$$

where $\hat{u}^*, \hat{v}^*, \hat{\eta}^*$, and $\hat{h}^*$ represent the dimensional cross-shore and longshore velocity, water suface elevation, and total water depth (including set-down/set-up), respectively, and the subscripts indicate derivatives in $x, y$, and $t$. For the modelling section we will adopt a coordinate system such that the $x$-axis is located along the centreline of the rip current and increasing in the offshore direction. The forcing due to radiation stress gradients, $\hat{R}^*_x$ and $\hat{R}^*_y$ (where the subscripts indicate the direction in which they act; same for $\hat{M}^*_x$, $\hat{M}^*_y$, $\hat{\mathscr{T}}^*_x$, and $\hat{\mathscr{T}}^*_y$), are defined dimensionally as

$$\hat{R}^*_x = -\frac{1}{\rho h}\left(\frac{\partial}{\partial x}\hat{S}^*_{xx} + \frac{\partial}{\partial y}\hat{S}^*_{yx}\right), \tag{3.4a}$$

$$\hat{R}^*_y = -\frac{1}{\rho h}\left(\frac{\partial}{\partial x}\hat{S}^*_{xy} + \frac{\partial}{\partial y}\hat{S}^*_{yy}\right), \tag{3.4b}$$

where $\hat{S}^*_{i,j}$ are the components of the radiation stress tensor and $\rho$ is the fluid density. The turbulent mixing terms, $\hat{M}^*_{x,y}$, are defined dimensionally as

$$\hat{M}^*_x = -\frac{1}{\rho h}\left(\frac{\partial}{\partial x}\hat{F}^*_{xx} + \frac{\partial}{\partial y}\hat{F}^*_{yx}\right), \tag{3.5a}$$

$$\hat{M}^*_y = -\frac{1}{\rho h}\left(\frac{\partial}{\partial x}\hat{F}^*_{xy} + \frac{\partial}{\partial y}\hat{F}^*_{yy}\right), \tag{3.5b}$$

where $\hat{F}^*_{\mathrm{i},j}$ are the components of the Reynolds stress tensor. Finally, $\hat{\mathscr{T}}^*_x$ and $\hat{\mathscr{T}}^*_y$ represent the bottom friction components.

We seek to model the development of the rip from an initial starting point. In this respect, we are not modelling the forcing of the rip directly, but instead we will treat the rip as an ambient free jet flow. In order to derive an analytical solution we will make certain simplifications. We will adopt the classical 'rigid-lid' approximation, $\hat{\eta}^*_t \approx 0$, and also assume a longshore uniform coast ($\hat{h}^* = \hat{h}^*(x)$). The first approximation is commonly used in the study of nearshore vorticity motions (see Falqués & Iranzo 1994 for a discussion), and the second is a reasonable starting point for the analysis of rip current dynamics and is not strictly violated within the rip current while it remains in the rip channel. This is essentially equivalent to assuming $\hat{\eta}^*_y = 0$.

We will also negelect the effects of wave–current interaction, such as wave refraction due to the opposing current, following Tam (1973). Instead, we will assume that in the $x$-direction the radiation stress forcing is balanced by the water surface gradient such that

$$g\hat{\eta}^*_x = \hat{R}^*_x, \tag{3.6}$$

and we will neglect the radiation stress forcing in the $y$-direction, $\hat{R}^*_y$. While it is certain that the rip current modifies the wave heights and the wave breaking in the

channel, the results of Yoon & Liu (1990) suggest that we may neglect the effects of radiation stress gradients on the evolution of the jet. Their numerical study indicates that the dominant processes driving jet spreading are bottom friction and turbulent mixing. Our purpose here is to obtain a reasonably simplified analytical solution for the rip current flow that contains the dominant physical mechanisms governing the rip dynamics, and, even more importantly, compares favourably with the measured mean data so that we can analyse the stability characteristics of the flow.

Using the above assumptions we cross-differentiate (3.1) and (3.2) and combine with (3.3) to obtain the dimensional, vorticity transport equation for a longshore uniform coast,

$$\frac{\mathrm{D}}{\mathrm{D}t}\left(\frac{\hat{u}_y^* - \hat{v}_x^*}{\hat{h}^*}\right) = -\frac{1}{\hat{h}^*}\nabla_h \times (\hat{\boldsymbol{M}}^* + \hat{\boldsymbol{\mathscr{T}}}^*), \tag{3.7}$$

where the horizontal gradient operator is defined such that $\nabla_h \times \hat{\boldsymbol{M}}^* = \partial \hat{M}_y^*/\partial x - \partial \hat{M}_x^*/\partial y$. In order to non-dimensionalize the above equation, we introduce the basic scales

$$\hat{u}^*, \hat{v}^* \sim U_0, \quad \hat{h}^* \sim h_0, \quad \hat{\boldsymbol{M}}^* \sim U_0^2/b_0,$$

$$x, y \sim b_0, \quad t \sim b_0/U_0, \quad \hat{\boldsymbol{\mathscr{T}}}^* \sim U_0^2/h_0,$$

where $U_0$ is a velocity scale, $b_0$ is a horizontal lengthscale, and $h_0$ is a depth scale. Substitution of the scales leads us to the following non-dimensional vorticity transport equation:

$$\frac{\mathrm{D}}{\mathrm{D}t}\left(\frac{\hat{u}_y - \hat{v}_x}{\hat{h}}\right) = -\frac{1}{\hat{h}}\nabla_h \times \hat{\boldsymbol{M}} + \frac{b_0}{h_0}\left(-\frac{1}{\hat{h}}\nabla_h \times \hat{\boldsymbol{\mathscr{T}}}\right), \tag{3.8}$$

($x, y, t$ are now also non-dimensional). We next assume our basic state is a steady mean flow with superimposed small disturbances such that

$$\hat{u}(x, y, t) = U(x, y) + u(x, y, t), \tag{3.9a}$$

$$\hat{v}(x, y, t) = V(x, y) + v(x, y, t), \tag{3.9b}$$

$$\hat{\boldsymbol{M}}(x, y, t) = \boldsymbol{M}^0(x, y) + \Delta\boldsymbol{M}(x, y, t), \tag{3.9c}$$

$$\hat{\boldsymbol{\mathscr{T}}}(x, y, t) = \boldsymbol{\mathscr{T}}^0(x, y) + \Delta\boldsymbol{\mathscr{T}}(x, y, t), \tag{3.9d}$$

where $U, V$ represent the steady mean flow, $u, v$ are the disturbance velocities, and $\boldsymbol{M}^0$ and $\boldsymbol{\mathscr{T}}^0$ represent the turbulent mixing and bottom stress in the absence of disturbances.

Equation (3.8), in the absence of disturbances (i.e. $u = v = 0$), can now be written as

$$U\left(\frac{U_y - V_x}{h}\right)_x + V\left(\frac{U_y - V_x}{h}\right)_y = -\frac{1}{h}\nabla_h \times \boldsymbol{M}^0 + \frac{b_0}{h_0}\left(-\frac{1}{h}\nabla_h \times \boldsymbol{\mathscr{T}}^0\right), \tag{3.10}$$

where $h = \hat{h}$ (non-dimensional water depth). This is the governing non-dimensional vorticity transport equation for steady flow.

Subtracting (3.10) from (3.8) and linearizing in the disturbance velocities, we obtain

$$\left(\frac{\partial}{\partial t} + U\frac{\partial}{\partial x} + V\frac{\partial}{\partial y}\right)\left(\frac{u_y - v_x}{h}\right) + \left(u\frac{\partial}{\partial x} + v\frac{\partial}{\partial y}\right)\left(\frac{U_y - V_x}{h}\right) = -\frac{1}{h}\nabla_h \times \Delta\boldsymbol{M} + \frac{b_0}{h_0}\left[-\frac{1}{h}\nabla_h \times \Delta\boldsymbol{\mathscr{T}}\right], \tag{3.11}$$

which represents the governing non-dimensional vorticity transport equation for the disturbed flow. Next, we will examine solutions to these equations by first specifying the form of the steady flow and then searching for growing solutions (instabilities) to the disturbance equation.

### 3.2. *Time-averaged flow*

Previous researchers have used simplified forms of (3.10) to model the mean flows in rip currents. For example, Arthur (1950) developed an analytical model that satisfied the inviscid form of (3.10) and matched the general characteristics of a rip current quite well. His model produced a long and narrow rip, supplied by nearshore feeder currents, which decayed in magnitude and spread laterally as it extended offshore. However, the rate of rip current spreading was essentially arbitrary and given without justification, and viscous effects were not considered. Tam (1973) determined a similarity solution to the rip current flow in a transformed coordinate system based on a boundary-layer analogy and investigated the influence of the bottom slope on the steady flow in the absence of bottom friction. His solution is mathematically equivalent to the Bickley jet (Bickley 1939). We will use a similar approach here; however, our approach is simpler as our coordinate system is more straightforward. We will also include the effects of bottom friction and compare to measured data. Our approach to the steady-flow problem will most resemble the approach of Joshi (1982), who analysed the hydromechanics of tidal jets. In contrast to Joshi (1982), we will approach the problem more generally in terms of a non-dimensional nearshore vorticity balance and apply the method of multiple scales, and also, we will present a simplified relationship for determining the empirical mixing and bottom friction coefficients from the experimental data.

The main purpose of this section is to develop a tractable model for the mean flows in a rip current so that we can investigate the stability characteristics of rip currents. Since the tidal jet model of Joshi contains the dominant mechanisms (turbulent mixing, bottom friction, variable bathymetry) governing the evolution of shallow water jets, we shall follow it closely. However, because the scales of tidal jets and rip currents are quite different, it will be important to test how well the modelled mean flows compare with the experimental data in order to verify the validity of the model for rip currents. We will also describe how the effects of turbulent mixing and bottom friction affect the rate of rip current spreading and the decay of rip velocities in the offshore direction so that we can subsequently interpret the results from the rip current instability model.

We will restrict our analysis of (3.10) to flows that are slightly non-parallel such that they are slowly varying in the cross-shore direction. Therefore, we introduce a scaled cross-shore coordinate $x_1$ such that

$$x_1 = \epsilon x, \tag{3.12}$$

where $\epsilon$ is a small dimensionless parameter that represents the slow variation of the flow. Thus, the steady-flow components are given by

$$U = U(x_1, y), \tag{3.13a}$$

$$V = \epsilon V(x_1, y), \tag{3.13b}$$

$$h = h(x_1), \tag{3.13c}$$

where (3.13*b*) indicates that the transverse velocity ($V(x, y)$) is finite but small before the coordinate transformation (i.e. slightly non-parallel flow). After substituting the

scaled coordinate, the left-hand side of (3.10) becomes

$$\epsilon U\left(\frac{U_y-\epsilon^2 V_{x_1}}{h}\right)_{x_1}+\epsilon V\left(\frac{U_y-\epsilon^2 V_{x_1}}{h}\right)_{y}=\text{R.H.S.} \tag{3.14}$$

Next, we must parameterize the turbulent mixing and bottom friction terms. It is common to neglect the normal Reynolds stress terms ($\hat{F}^*_{xx}$, $\hat{F}^*_{yy}$) since they are generally small. We shall parameterize the remaining terms using Prandtl's 'apparent kinematic viscosity' hypothesis with a turbulent eddy viscosity, $\nu_T$, such that the non-dimensional turbulent mixing terms take the following forms

$$\hat{M}_x=\frac{1}{\hat{h}}\frac{\partial}{\partial y}(\hat{h}\,\hat{\nu}_T\,\hat{u}_y), \tag{3.15a}$$

$$\hat{M}_y=\frac{1}{\hat{h}}\frac{\partial}{\partial x}(\hat{h}\,\hat{\nu}_T\,\hat{u}_y). \tag{3.15b}$$

After introducing the scaled coordinate, the mixing in the absence of disturbances takes the forms

$$M^0_{x_1}=\frac{1}{R_t}\frac{\partial}{\partial y}(U_m\ell\,U_y), \tag{3.16a}$$

$$M^0_{y}=\frac{\epsilon}{R_t}\frac{1}{h}\frac{\partial}{\partial x_1}(h\,U_m\ell\,U_y), \tag{3.16b}$$

where $R_t$ is a constant non-dimensional turbulent Reynolds number defined as $R_t\equiv U_m\ell/\nu_T$, $\ell$ is a mixing length, and $U_m$ represents the velocity at the rip current centreline and varies in the cross-shore direction. For the bottom friction, we will use the following nonlinear formulations

$$\hat{\mathscr{F}}_x=-\frac{f_d}{8\hat{h}}\,\hat{u}\,|\hat{\boldsymbol{u}}|, \tag{3.17a}$$

$$\hat{\mathscr{F}}_y=-\frac{f_d}{8\hat{h}}\,\hat{v}\,|\hat{\boldsymbol{u}}|, \tag{3.17b}$$

where $f_d$ is a Darcy–Weisbach friction factor and $\hat{\boldsymbol{u}}$ is the total current vector. In the absence of disturbances, the scaled variables for the bottom friction terms become

$$\mathscr{F}^0_{x_1}=-\frac{f_d}{8\,h}U(U^2+\epsilon^2\,V^2)^{1/2}, \tag{3.18a}$$

$$\mathscr{F}^0_{y_1}=-\frac{\epsilon f_d}{8\,h}V(U^2+\epsilon^2 V^2)^{1/2}. \tag{3.18b}$$

It is evident, since the terms in (3.14) are $O(\epsilon)$ or smaller, that the parameter $1/R_t$ in (3.16) must be at least as large as $O(\epsilon)$ in order to retain the effects of turbulent mixing on the time-averaged flow. Therefore, we will retain $M^0_{x_1}$ and neglect the smaller term $M^0_{y_1}$. Likewise, we take the non-dimensional frictional parameter $f_t\equiv f_d b_0/8h_0$ to be $O(\epsilon)$, and therefore retain $\mathscr{F}^0_{x_1}$ and neglect $\mathscr{F}^0_{y_1}$. The governing equation for the time-averaged rip current flow can then be written as

$$UU_{yx_1}-UU_y\frac{h_{x_1}}{h}+VU_{yy}=\frac{1}{R_t}\left(U_m\ell\,U_{yyy}\right)-f_t\left(\frac{2UU_y}{h}\right). \tag{3.19}$$

We will treat the rip current as a self-preserving turbulent jet. The self-preservation

of the jet implies that the evolution of the flow is governed by local scales of length and velocity (Tennekes & Lumley 1972). We will take the local lengthscale to be $\ell = b(x_1)$, the half-width of the jet, and the velocity scale, $U_m(x_1)$, to be the local velocity at the jet centreline. In addition, if the jet is self-preserving, the dimensionless velocity profiles $U/U_m$ at all $x_1$ locations will be identical when plotted against the dimensionless coordinate $y/b$. Therefore, we introduce a similarity variable

$$\eta = \frac{y}{b(x_1)}, \tag{3.20}$$

and we assume that

$$\frac{U(x_1, y)}{U_m(x_1)} = f(\eta) \quad \text{only.} \tag{3.21}$$

It is important to note here that $y$ was previously non-dimensionalized by the constant $b_0$, which we have defined as the jet width at the origin. The jet width $b(x_1)$ has also been non-dimensionalized by $b_0$, and therefore $b(0) = 1$. Similarly, the velocities have been non-dimensionalized by $U_0$ which we have defined as the maximum velocity at the origin, therefore $U_m(0) = 1$.

In order to write (3.19) in terms of similarity variables, we must first obtain an expression for $V(x_1, \eta)$. We do this by integrating the non-dimensional form of (3.3) from 0 to $y$ at a given $x_1$, using the condition of zero transverse flow at the jet centreline ($V(x_1, \eta = 0) = 0$), to obtain

$$V = U_m b_{x_1} \eta f - \left( U_{m_{x_1}} b + U_m \frac{h_{x_1}}{h} b + U_m b_{x_1} \right) \int_0^\eta f \, \mathrm{d}\eta'. \tag{3.22}$$

For the mixing term we will assume self-preservation of the Reynolds stress such that we can express the mixing as

$$\frac{1}{R_t} U_m \ell \, U_y = U_m^2 \, g(\eta), \tag{3.23}$$

where $g(\eta)$ is an as yet unspecified similarity function.

Substitution of the similarity forms of the velocities and Reynolds stress into (3.19) and simplifying, leads us to the following

$$\left( \frac{b \, U_{m_{x_1}}}{U_m} - b_{x_1} - \frac{b \, h_{x_1}}{h} + 2\frac{f_t \, b}{h} \right) f f_\eta - \left( \frac{b \, U_{m_{x_1}}}{U_m} + \frac{b \, h_{x_1}}{h} + b_{x_1} \right) f_{\eta\eta} \int_0^\eta f \, \mathrm{d}\eta' = g_{\eta\eta}, \tag{3.24}$$

where subscripts $\eta$ and $x_1$ represent derivatives. Note that $f$ and $g$ do not depend explicitly on $x_1$, whereas the coefficients on the left-hand side of (3.24) are generally functions of $x_1$. Therefore, for this equation to hold throughout the region of study, the coefficients must be independent of $x_1$. If we alternately add and subtract these two relations (the expressions in parentheses in (3.24)), we obtain the following equations governing the length and velocity scales

$$b_{x_1} + \left( \frac{h_{x_1}}{h} - \frac{f_t}{h} \right) b = C, \tag{3.25}$$

$$U_{m_{x_1}} + \left( \frac{f_t}{h} - \frac{C_1}{b} \right) U_m = 0, \tag{3.26}$$

where $C$ and $C_1$ are true constants. These equations can be solved by the method of variation of parameters (see e.g. Greenberg 1988 pp. 907–909) to obtain the following

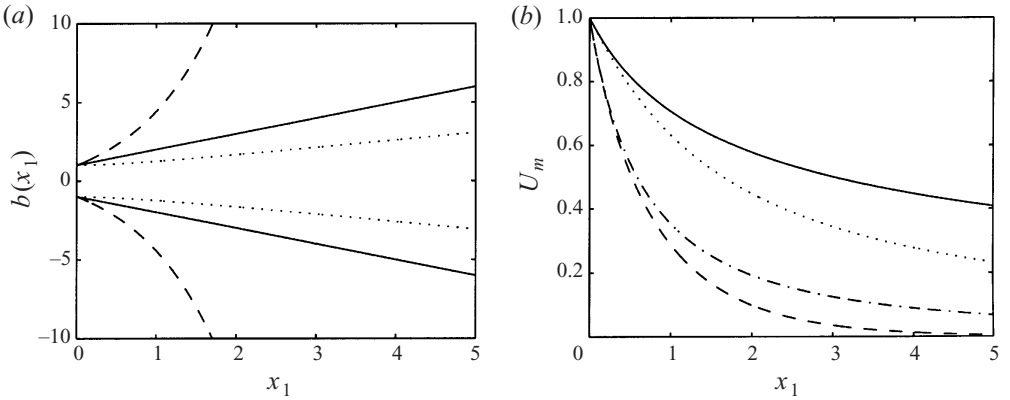


FIGURE 13. Cross-shore variation of the rip current scales (*a*) jet width *vs.* cross-shore distance (*b*) centreline velocity *vs.* cross-shore distance for —, classical plane jet, - - -, flat bottom w/friction ($f_t = 1$), $\cdots$, planar beach ($m_1 = 1$, $f_t = 0$), ---, frictional planar beach ($m_1 = f_t = 1$) (dash-dot is on top of solid line in (*a*).

general solutions for the width and velocity scales of the jet

$$b(x_1) = \frac{1}{h(x_1)} \exp\left(f_t \int_0^{x_1} h^{-1} \mathrm{d}\xi\right) \left[1 + C \int_0^{x_1} h(\xi_1) \exp\left(-f_t \int_0^{\xi_1} h^{-1} \mathrm{d}\zeta\right) \mathrm{d}\xi_1\right], \tag{3.27}$$

$$U_m(x_1) = C_3 \exp\left(-f_t \int_0^{x_1} h^{-1}\, \mathrm{d}\xi\right) \left[1 + C \int_0^{x_1} h(\xi_1) \exp\left(-f_t \int_0^{\xi_1} h^{-1}\, \mathrm{d}\zeta\right) \mathrm{d}\xi_1\right]^{C_1/C}, \tag{3.28}$$

where the lower limit of integration has been chosen to be $x_1 = 0$, also the non-dimensional depth at the origin has been specified as $h(0) = 1$; thus, $C, C_1$, and $C_3$ are the three constants we are left to evaluate. The relationships between the constants $(C, C_1, C_3, R_t)$ and the functional form of $f$ are given in Appendix B.

For a frictionless flat bottom, (3.27) and (3.28) collapse to the classical plane jet solution whereby the width scale grows linearly along the jet axis and the centreline velocity decays with $x^{-1/2}$. Figure 13 shows the variation of the width scale and the centreline velocity in the offshore direction for specific parameter values. It can be seen that friction increases the jet spreading and causes the centreline velocity to decay more rapidly. In contrast, the jet spreading is reduced by an increasing depth in the offshore direction owing to vortex stretching (Arthur 1962). In addition, if the frictional spreading effects are balanced by the narrowing due to vortex stretching ($f_t = m_1$), then the jet spreads linearly at the same rate as the classical plane jet. These results are equivalent to those described by Joshi (1982) for the tidal jet.

### 3.2.1. *Comparison to data*

Next, we compare the results from our model for rip current mean flows with the measured velocity profiles from the experiments. For the comparison, we adopt a new cross-shore coordinate axis $x' = x_0 - x$ where $x_0$ is the cross-shore location (dimensional) of the base of the rip current during the experiments. Thus, $x'$ is now increasing in the offshore direction and the location of the jet origin, $x_0$, is determined as the experimental location where the rip begins to exhibit decay of its centreline velocity and is different for each test. The location of the rip current centreline, $y_0$, is

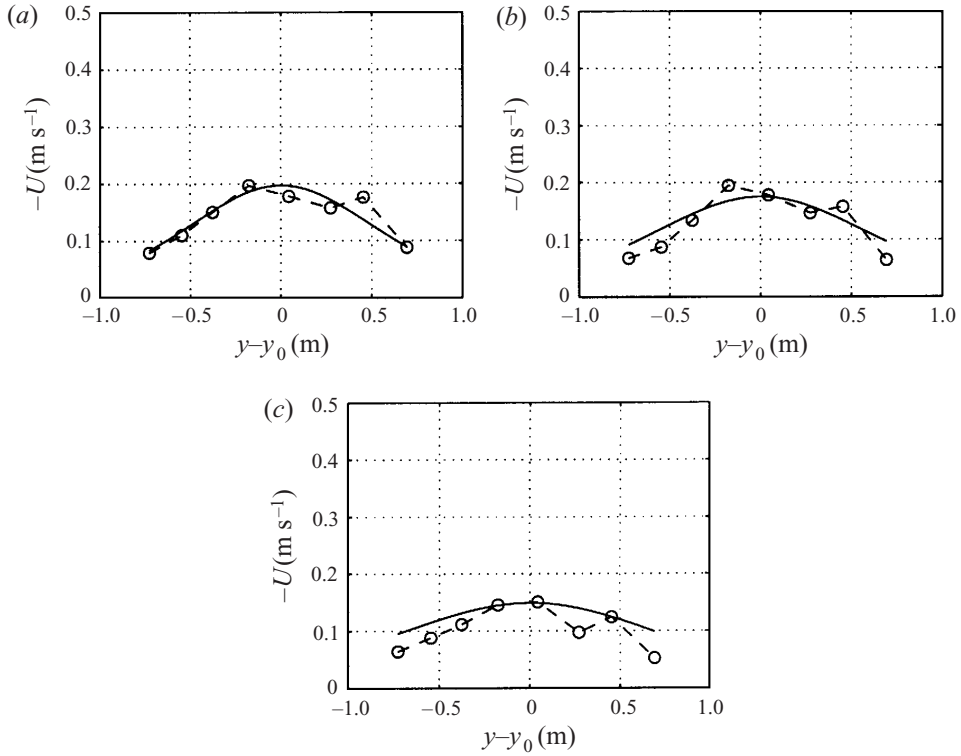


FIGURE 14. Comparison of best fit mean rip current velocity profile to experimental data for test B (*a*) $x' = 0\,\mathrm{m}$ ($x = 11.94\,\mathrm{m}$), (*b*) $x' = 0.2\,\mathrm{m}$ ($x = 11.74\,\mathrm{m}$), (*c*) $x' = 0.5\,\mathrm{m}$ ($x = 11.44\,\mathrm{m}$).

determined by taking a weighted average of the mean rip current velocities measured at the jet origin. This is given by

$$y_0 = \frac{\sum_{i=1}^{N} U(i)y(i)\Delta y(i)}{\sum_{i=1}^{N} U(i)\Delta y(i)}, \tag{3.29}$$

where $N$ is the number of observations made at the jet origin.

Once $x_0$ and $y_0$ were determined, the choices of the dimensional velocity and width scales, $U_0$ and $b_0$, respectively, were made by a fitting procedure performed using the rip velocity profile at the origin. The statistical parameter we use to determine the best fit of the modelled velocity profile to the experimental data is the index of agreement $d_i$ that was proposed by Wilmott (1981) and is given by

$$d_i = 1 - \frac{\sum_{i=1}^{N} (\beta(i) - \alpha(i))^2}{\sum_{i=1}^{N} (|\beta(i) - \bar{\alpha}| + |\alpha(i) - \bar{\alpha}|)^2}, \tag{3.30}$$

where $\alpha(i)$ and $\beta(i)$ are the measured and model data, respectively, and $\bar{\alpha}$ is the measured data mean. This parameter varies between 0 and 1 with $d_i = 1$ representing complete agreement. The scales $U_0$ and $b_0$ were then determined by a search procedure

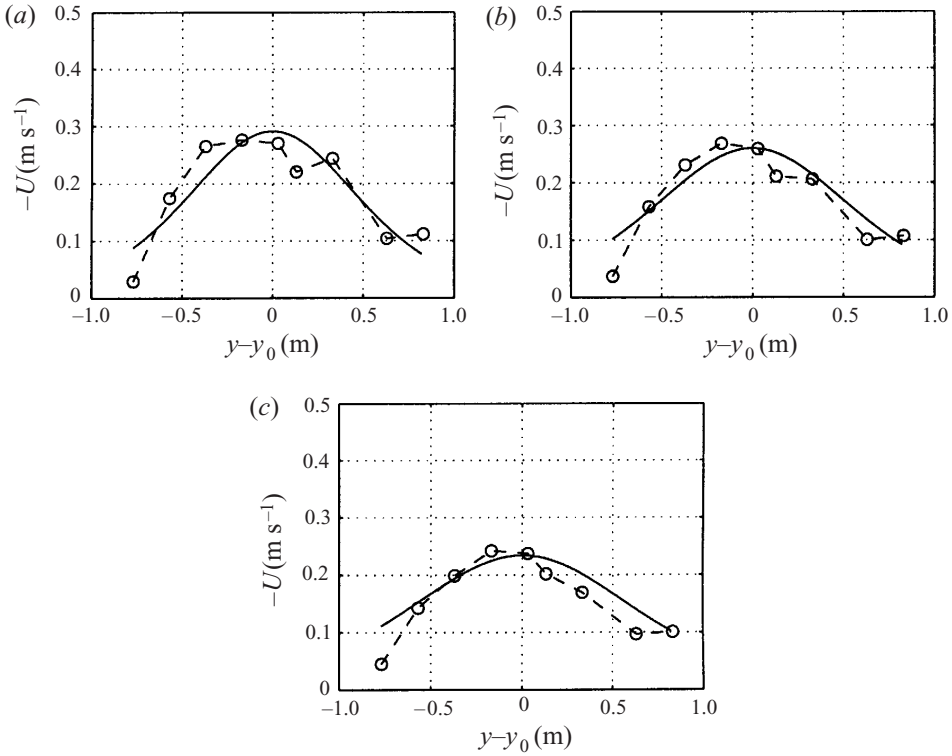


FIGURE 15. Comparison of best fit mean rip current velocity profile to experimental data for test C (*a*) $x' = 0$ m ($x = 11.63$ m), (*b*) $x' = 0.2$ m ($x = 11.43$ m), and (*c*) $x' = 0.4$ m ($x = 11.23$ m).

| Test | $x_0$ (m) | $y_0$ (m) | $U_0$ (cm s$^{-1}$) | $b_0$ (cm) | $d_i$ | $R_t$ | $f_t$ | $d_i'$ |
|---|---|---|---|---|---|---|---|---|
| B | 11.94 | 13.68 | 19.7 | 73 | 0.96 | 4.25 | 0.48 | 0.88 |
| C | 11.63 | 13.57 | 29.1 | 64 | 0.94 | 4.75 | 0.48 | 0.90 |
| D | 11.43 | 13.74 | 49.0 | 62 | 0.91 | — | — | — |
| E | 11.93 | 13.8 | 28.4 | 52 | 0.94 | 2.5 | 0.46 | 0.94 |
| G | 11.93 | 13.68 | 23.4 | 71 | 0.95 | 2.75 | 0.44 | 0.97 |

TABLE 3. Table of rip current scales determined by parameter search procedure, $x_0$ cross-shore location of rip current origin, $y_0$ longshore location of rip current centreline, $U_0$ velocity scale, $b_0$ width scale, $d_i$ index of agreement for velocity profile at origin, $R_t$ turbulent Reynolds number, $f_t$ bottom friction parameter, $d_i'$ index of agreement velocity along rip centreline.

where the index of agreement was computed for a large range of possible scales ($\Delta U_0 = 0.1$ cm s$^{-1}$, $\Delta b_0 = 1$ cm) and the best fit was chosen from the maximum value of $d_i$.

The mixing and friction scales $R_t$ and $f_t$ were also determined by a similar procedure. It is evident from (B 5) and (B 10) that the decay of the centreline velocity is directly related to the values of $R_t$ and $f_t$. Therefore, these parameters were determined by fitting the decay of the centreline velocity between the model and data using a parameter search with a resolution of $\Delta R_t = 0.25$ and $\Delta f_t = 0.0093$. Since the experimental data points were never located at the exact centreline of the rip the model/data comparison was made with the data points located closest to the centreline.

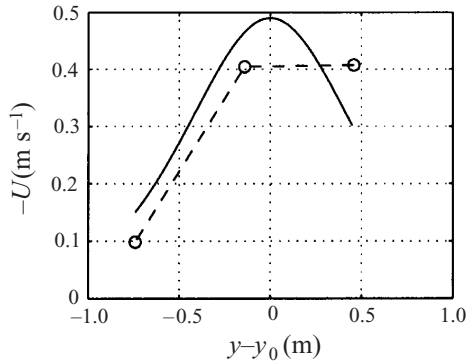


FIGURE 16. Comparison of best fit mean rip current velocity profile to experimental data for test D, $x' = 0\,\mathrm{m}$ ($x = 11.43\,\mathrm{m}$).

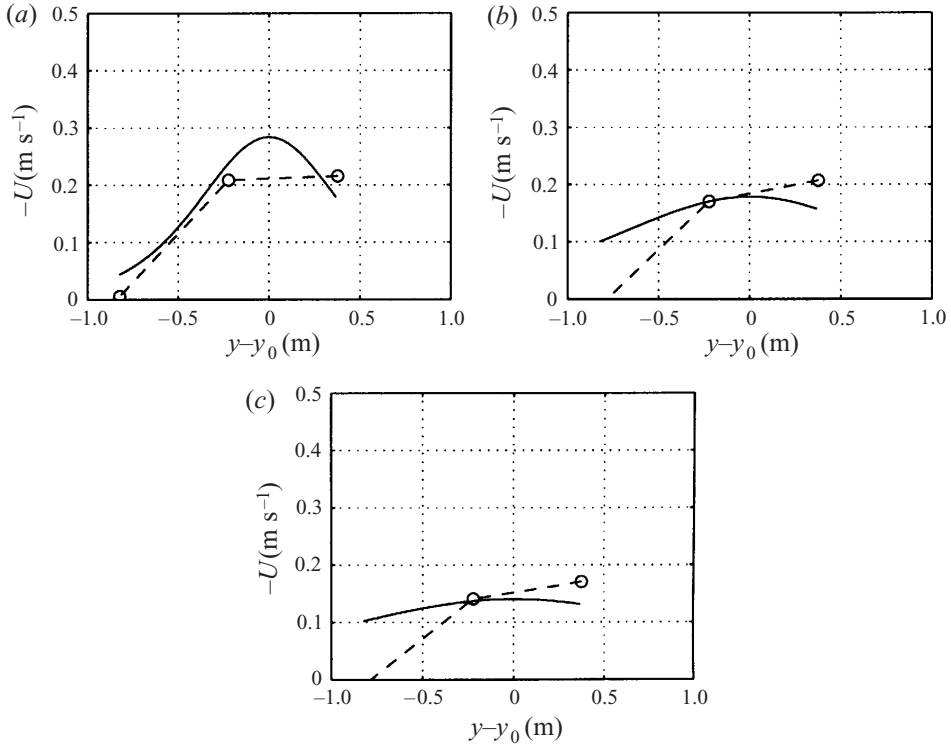


FIGURE 17. Comparison of best-fit mean rip current velocity profile to experimental data for test E (*a*) $x' = 0\,\mathrm{m}$ ($x = 11.93\,\mathrm{m}$), (*b*) $x' = 0.3\,\mathrm{m}$ ($x = 11.63\,\mathrm{m}$), (*c*) $x' = 0.5\,\mathrm{m}$ ($x = 11.43\,\mathrm{m}$).

The best-fit modelled velocity profiles are shown in figures 14–18. The dimensional scales and the index of agreement for each test are listed in table 3. No estimate of $R_t$ and $f_t$ could be made for test D since the decay of the rip current velocity is not captured by the measurements. The best-fit values for the friction factor $f_d$ ($f_d = 8f_t h_0/b_0$) are at least an order of magnitude higher than those normally found on field beaches, however, they compare well with those used in the modelling of longshore currents in the laboratory (Kobayashi, Karjadi & Johnson 1997). Also, the best fit values of $R_t$ are found to be significantly lower than those reported previously

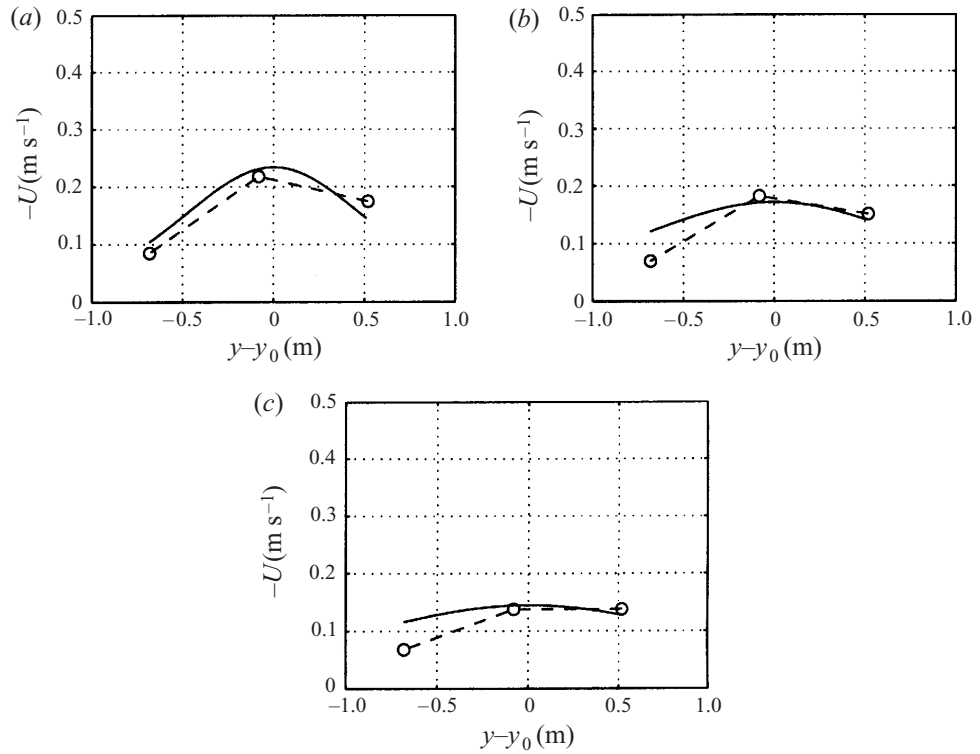


FIGURE 18. Comparison of best-fit mean rip current velocity profile to experimental data for test G (*a*) $x' = 0$ m ($x = 11.93$ m), (*b*) $x' = 0.3$ m ($x = 11.63$ m), (*c*) $x' = 0.5$ m ($x = 11.43$ m).

for plane jets, which have suggested $R_t \approx 25$. The present results indicate that the rip current has a faster spreading rate than a traditional plane jet. This is probably a direct result of the increased importance of non-parallel effects (turbulent mixing and bottom friction) in rip current flows. An additional source of turbulent mixing, not directly considered here, is the presence of instabilities of finite amplitude. This will be discussed further with regard to the linear stability model in § 3.3. Finally, the tabulated values of the index of agreement show that the model was reasonable in fitting to the measured profiles, since the index of agreement is at least 0.88 for all cases. However, it should be noted that for many of the tests there were only three data points for comparison, which is a very small number.

### 3.3. *Linear stability analysis*

Next, we derive a linear stability model for the viscous turbulent jet. Returning to the governing equation for the disturbed flow (3.11) and substituting the mixing parameterization (3.16), we have the following expressions for the mixing in the presence of disturbances:

$$\Delta M_x = \frac{1}{R_t}\frac{\partial}{\partial y}(U_m\, b\, u_y), \tag{3.31a}$$

$$\Delta M_y = \frac{1}{hR_t}\frac{\partial}{\partial x}(h\, U_m\, b\, u_y). \tag{3.31b}$$

Likewise, using the bottom friction parameterization (3.18) the bottom stress terms in the presence of disturbances become

$$\Delta\mathscr{T}_x = -\frac{f_d}{8h}(U+u)|\boldsymbol{U}+\boldsymbol{u}| + \frac{f_d}{8h}U|\boldsymbol{U}|, \tag{3.32a}$$

$$\Delta\mathscr{T}_y = -\frac{f_d}{8h}(V+v)|\boldsymbol{U}+\boldsymbol{u}| + \frac{f_d}{8h}V|\boldsymbol{U}|, \tag{3.32b}$$

where $\boldsymbol{U}$ and $\boldsymbol{u}$ are the steady and disturbance current vectors, respectively.

Using (3.3) we can introduce a stream function $\psi(x, y, t)$ for the disturbances, such that

$$\psi_y = uh, \tag{3.33a}$$

$$-\psi_x = vh. \tag{3.33b}$$

We then consider a normal-mode analysis of (3.11) and assume a harmonic dependence on $x$ and $t$, so the stream function takes the form

$$\psi(x, y, t) = \phi(y)\,\mathrm{e}^{\mathrm{i}(kx-\omega t)}, \tag{3.34}$$

and the eigenfunction $\phi$ contains the transverse structure of the instabilities.

At this point there are two ways to approach the instability eigenvalue problem. The first approach is to seek unstable modes that grow in time from disturbances at a given wavenumber. This temporal instability approach assumes that the wavenumber, $k \equiv 2\pi/L$, is real and the eigenvalue, $\omega$, is in general complex with the real part, $\omega_r$, being the angular frequency, and the imaginary part, $\omega_i$, being the temporal growth rate. From inspection of (3.34), it is evident that a given mode is linearly unstable if $\omega_i > 0$, since the mode will then grow in time. Of course, in practice, neglected nonlinear effects will restrict growth at some finite value.

The second approach seeks unstable modes that grow spatially with propagation distance from an initial disturbance at a given frequency. Conversely, the spatial instability approach assumes $\omega$ to be purely real and the eigenvalue $k$ is, in general, complex with $k_r$ representing the wavenumber $(2\pi/L)$ and $k_i$ the spatial growth rate. A given mode is linearly unstable when $k_i < 0$ and will grow as it propagates downstream with the mean current $U$.

The spatial theory is a better representation of the physical experiments, since the disturbances must be initiated locally at the upstream end of the current, and grow downstream. Also, the temporal theory assumes an initial disturbance that is uniform in the cross-shore direction and is, therefore, not valid here since the mean flow is spatially varying in the cross-shore direction. A discussion of the results of temporal jet instability theory as applied to the rip current problem can be found in Haller & Dalrymple (1999). In the following analysis, we will consider only spatially growing instabilities.

In order to account for the non-parallel nature of the flow in the stability analysis, we will use the method of multiple scales in a similar fashion to Nayfeh, Saric & Mook (1974) who applied it to boundary-layer flows. Assuming $\epsilon$ to be small, we expand the disturbance stream function $\psi$ in the following form

$$\psi(x_1, y, t) = [\phi_0(x_1, y) + \epsilon\phi_1(x_1, y)]\,\mathrm{e}^{\mathrm{i}\theta}, \tag{3.35}$$

where

$$\frac{\partial\theta}{\partial x} = k_0(x_1), \quad \frac{\partial\theta}{\partial t} = -\omega, \tag{3.36}$$

with the real part of $k_0$ being the non-dimensional wavenumber, the imaginary part being the growth rate and $\omega$ is the non-dimensional frequency.

In terms of $x_1$ and $\theta$, the spatial and temporal derivatives transform according to

$$\frac{\partial}{\partial x} = k_0(x_1)\frac{\partial}{\partial \theta} + \epsilon\frac{\partial}{\partial x_1}, \tag{3.37a}$$

$$\frac{\partial}{\partial t} = -\omega\frac{\partial}{\partial \theta}, \tag{3.37b}$$

therefore, the fast scale describes the axial variation of the travelling-wave disturbances and the slow scale is used to describe the relatively slow variation of the wavenumber, growth rate, and disturbance amplitude.

Substituting the assumed stream function and the mixing and bottom stress parameterizations into the governing equation we then separate the terms by order in $\epsilon$. The governing equation at order $\epsilon^0$ is given by

$$\left(U - \frac{\omega}{k}\right)(\phi_{0_{yy}} - k_0^2\phi_0) - \phi_0 U_{yy} = 0, \tag{3.38}$$

or

$$\mathscr{L}(\phi_0) = 0,$$

which is the Rayleigh stability equation. The non-parallel effects appear in the $O(\epsilon)$ equation which is given by

$$\mathscr{L}(\phi_1) = d_1\phi_{0_{x_1}} + d_2\phi_{0_{x_1yy}} + d_3\phi_{0_y} + d_4\phi_{0_{3y}} + d_5\phi_0 + d_6\phi_{0_{yy}} + d_7\phi_{0_4y}, \tag{3.39}$$

and the coefficients are given in Appendix C.

The eigenvalue problem defined by (3.38) (with $U(x_1, y)$ given by (3.19)) can be solved numerically to determine the eigenvalue $k_0$ for a given $\omega$. In order to solve the inhomogeneous second-order problem we must first determine $k_{x_1}$ and $\phi_{0_{x_1}}$. We can derive an expression for $\phi_{0_{x_1}}$ by differentiating (3.38) with respect to $x_1$, and we obtain after simplification

$$\mathscr{L}(\phi_{0_{x_1}}) = A_1 + k_{0_{x_1}}A_2, \tag{3.40}$$

where the coefficients are given by

$$A_1 = (U_{yyx_1} + k_0^2 U_{x_1})\phi_0 - U_{x_1}\phi_{0_{yy}},$$
$$A_2 = (2k_0U - \omega)\phi_0 - \frac{\omega}{k_0^2}\phi_{0_{yy}}.$$

The inhomogeneous equation governing $\phi_{0_{x_1}}$ has a solution if, and only if, the inhomogeneous terms are orthogonal to every solution of the adjoint homogeneous problem. This constraint is expressed as

$$\int_{-\infty}^{\infty}(A_1 + k_{0_{x_1}}A_2)\,\phi_0^*\,\mathrm{d}y = 0, \tag{3.41}$$

where $\phi_0^*$ is the eigenfunction from the adjoint eigenproblem given by

$$(U - c)\phi^*_{0_{yy}} + 2U_y\phi^*_{0_y} - k^2(U - c)\phi_0^* = 0. \tag{3.42}$$

Equation (3.41) can be rearranged to give the following expression for the derivative of the wavenumber

$$k_{0_{x_1}} = -\frac{\displaystyle\int_{-\infty}^{\infty} A_1\,\phi_0^*\,\mathrm{d}y}{\displaystyle\int_{-\infty}^{\infty} A_2\,\phi_0^*\,\mathrm{d}y}. \tag{3.43}$$

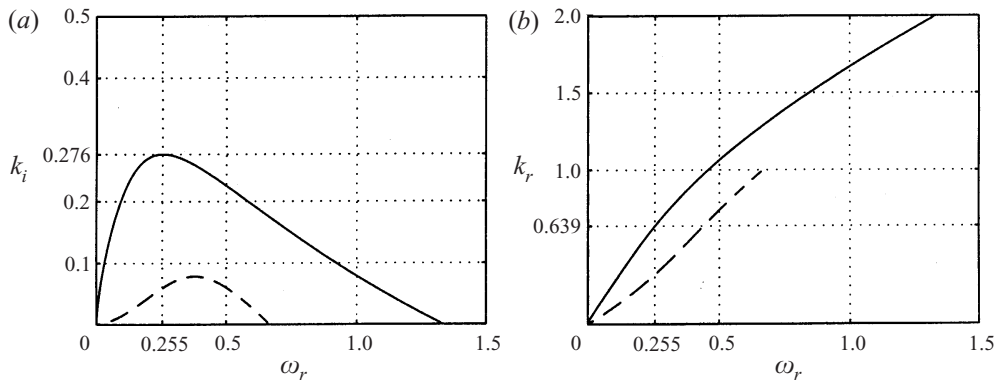


FIGURE 19. (*a*) Spatial growth rate *vs.* frequency and (*b*) wavenumber *vs.* frequency for the parallel turbulent jet. —, sinuous modes; - - -, varicose modes; all variables are non-dimensional.

Once $k_{0_{x_1}}$ is known, (3.40) can be integrated to obtain $\phi_{0_{x_1}}$.

Finally, the complex wavenumber including non-parallel effects is given (to order $\epsilon$) by

$$k \equiv (k_0 + \epsilon k_1), \tag{3.44}$$

where $k_1$ is given in Appendix C, and $k_i$ is now the local growth rate and $k_r$ the local wavenumber. The small parameter $\epsilon$ is the ratio between the longshore and cross-shore velocity scales or $V_{max}/U_{max}$, which for the viscous, turbulent jet is

$$\epsilon \equiv \frac{V_{max}}{U_{max}} = \frac{2}{R_t}. \tag{3.45}$$

### 3.3.1. *Model results*

A reasonable first estimate of the instability scales of the rip current is given by the zeroth-order stability equation (3.38), these results correspond to the results from a purely parallel flow theory. The solutions fall into two categories, *sinuous* or *varicose*, depending on whether $\psi$ is an even or odd function of $y$, respectively. The spatial instability curve and dispersion relation (zeroth-order solution) for the rip current disturbances are shown in figure 19 for both the sinuous and varicose modes. As a check on these results, the temporal stability curves were calculated from the spatial results using Gaster's relations (Gaster 1962). The temporal results, calculated in this manner, are in excellent agreement with the directly computed temporal results of Drazin & Howard (1966) who studied the Bickley jet ($U = \mathrm{sech}^2(y)$). The corresponding flow vectors of the parallel jet including the instabilities (FGM) are shown in figure 20.

The spatial results, shown in figure 19, indicate that the sinuous modes have the highest growth rates, and the fastest growing sinuous mode (FGM) has non-dimensional frequency $\omega = 0.255$, wavenumber $k_r = 0.639$, and phase speed ($C = \omega/k_r$) that is nearly 40% of the maximum jet velocity. It is interesting to note that there is a large difference between the scales of the spatial FGM and the temporal FGM ($\omega_r = 0.46$, $k = 1.0$). Therefore, unlike many other instabilities (e.g. longshore current instabilities, see Dodd & Falqués 1996) the temporal theory, in the rip current case, cannot be assumed to apply for spatially growing disturbances. However, the spatial results can be calculated accurately from the temporal results using Gaster's relations at this level of approximation.

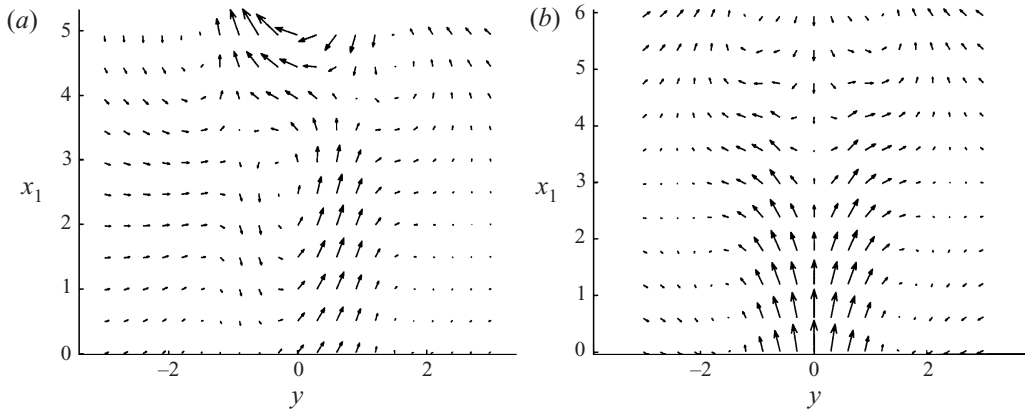


FIGURE 20. Flow vectors of the parallel turbulent jet including the instability (FGM) for (*a*) sinuous mode, (*b*) varicose mode, the amplitude of the instability is arbitrary and has been chosen such that the flow pattern is easily visualized.

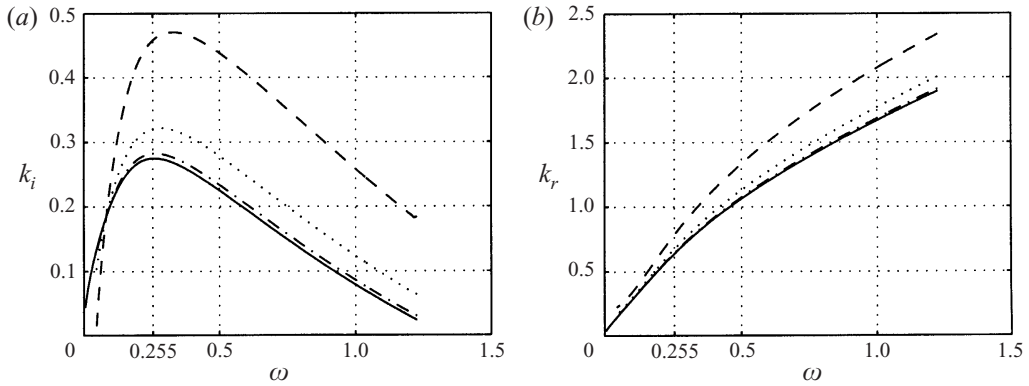


FIGURE 21. (*a*) Growth rate *vs.* frequency (*b*) wavenumber *vs.* frequency for different turbulent Reynolds numbers, - - -, $R_t = 5$; $\cdots$, $R_t = 10$; ---, $R_t = 25$; —, parallel flow, all variables are non-dimensional and results are for flat bottom and $f_t = x_1{=}0$ (sinuous mode only).

Since at this level of approximation, the stability scales are not a function of $R_t$, $h$, or $f_t$, we will have to move to the next order (3.39) in order to investigate the non-parallel effects due to turbulent mixing, vortex stretching, and bottom friction, respectively. Additionally, we will restrict our analysis to the sinuous mode since it exhibits the fastest growth rate. Figure 21 demonstrates the effect of turbulent mixing on the rip current jet instability. From this figure we can see that the initial growth rates increase inversely with $R_t$, and the frequency of the FGM also increases slightly with lower $R_t$. In addition, the phase speeds vary directly with $R_t$, such that lower $R_t$ causes slower phase speeds. These results are mostly explained by the fact that the magnitude of the non-parallel effects (i.e. $\epsilon$) is proportional to $1/R_t$. Physically, the increased growth rates are a direct result of the increased inflow ($V$) into the jet, the increased inflow also causes the disturbances to propagate at a slower speed. These results are consistent with those of Garg & Round (1978) who analysed the effects of viscous stresses in laminar jet flows. It is also evident that at very high values of $R_t$ the solutions collapse to the parallel flow values (solid lines).

Figure 22 shows the effect of bottom friction on the instabilities. The figure indicates

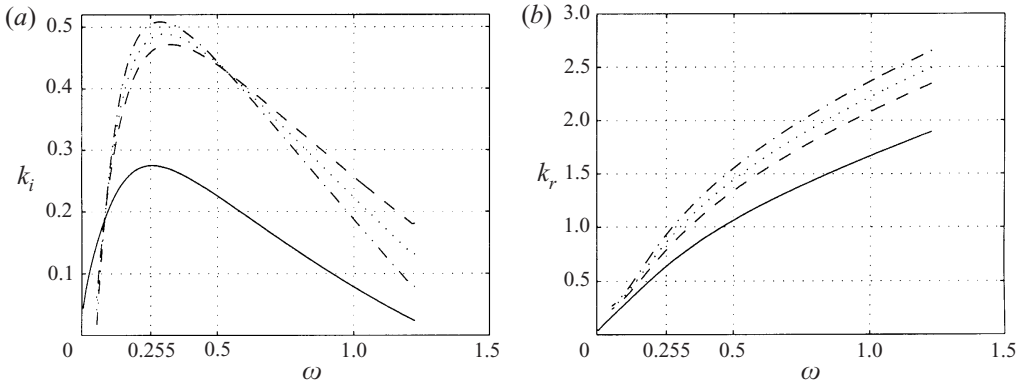


FIGURE 22. (*a*) Growth rate *vs.* frequency, (*b*) wavenumber *vs.* frequency for different values of bottom friction, - - -, $f_t = 0.01$; $\cdots$, $f_t = 0.2$; -·-, $f_t = 0.4$; —, parallel flow, all variables are non-dimensional and results are for flat bottom, $x_1$=0, and $R_t = 5$ (sinuous mode only).

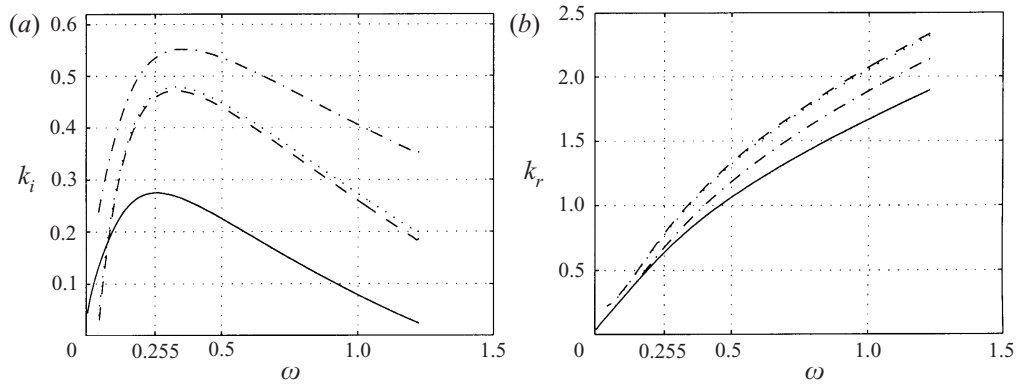


FIGURE 23. (*a*) Growth rate *vs.* frequency, (*b*) wavenumber *vs.* frequency for different bottom slopes, -·-·-, $m_1 = 0.001$; $\cdots$, $m_1 = 0.01$; - - -, $m_1 = 0.1$; —, parallel flow $m_1 = 0$, all variables are non-dimensional, $f_t = 0$ and $R_t = 5$.

that increased bottom frictional dissipation causes an increase in the initial growth rates and a decrease in the range of unstable frequencies. The increased growth rates are due to the effect of the decay of the centreline velocity. Essentially, since with increased bottom friction the jet initially spreads very quickly, the inflow is initially much stronger and therefore the jet is more unstable. Additionally, the increased bottom friction causes the disturbances to propagate more slowly, as can be seen by the dispersion curves. The results collapse to those for $f_t = 0$ and $R_t = 5$ (figure 21) for very low friction.

Figure 23 shows the effects of different bottom slopes on the instabilities. The results indicate that increased bottom slope increases the growth rates at $x_1 = 0$. This is related to the effects of vortex stretching and of spatial deceleration of the rip current. Though the jet does not spread as quickly on a sloping beach compared to a flat bottom owing to vortex stretching, the centreline velocity decays more quickly with increased beach slope owing to continuity effects. This increased spatial deceleration causes the growth rates to increase. Also, the phase speeds of the disturbances increase on the relatively narrower jets of planar beaches.

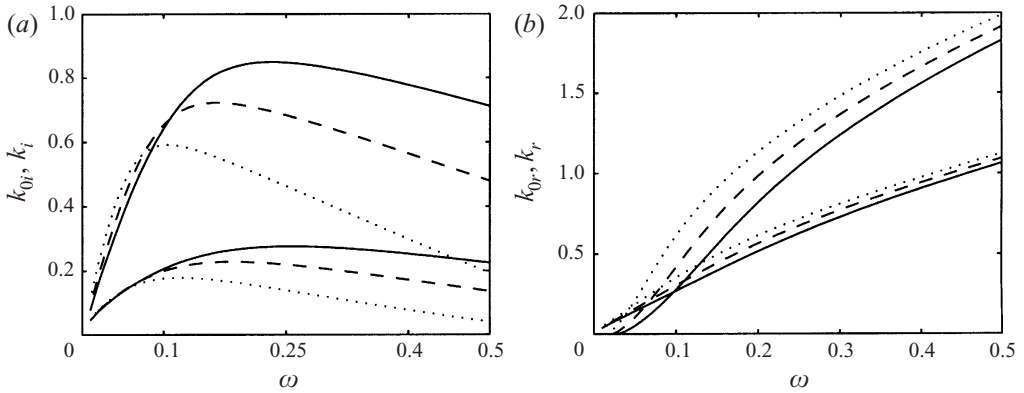


FIGURE 24. (*a*) Growth rate *vs.* frequency, (*b*) wavenumber *vs.* frequency for test B, all variables are non-dimensional. —, $x' = 0\,\mathrm{m}$; - - -, $x' = 0.2\,\mathrm{m}$; $\cdots$, $x' = 0.5\,\mathrm{m}$, upper curves include non-parallel effects ($k$), lower curves are for parallel flow theory ($k_0$).

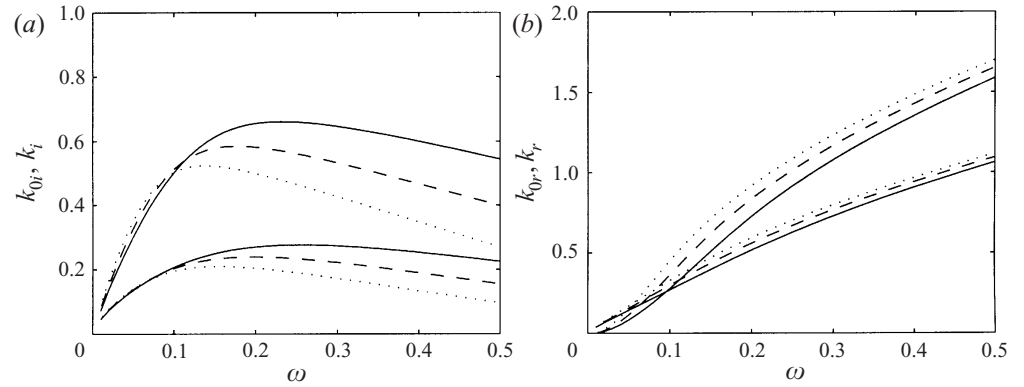


FIGURE 25. (*a*) Growth rate *vs.* frequency, (*b*) wavenumber *vs.* frequency for test C, all variables are non-dimensional. —, $x' = 0$; - - -, $x' = 0.2\,\mathrm{m}$; $\cdots$, $x' = 0.4\,\mathrm{m}$, upper curves include non-parallel effects ($k$), lower curves are for parallel flow theory ($k_0$).

### 3.3.2. *Model/data comparison*

With the rip scales listed in table 3, we can now use the stability model to investigate the instability characteristics of the experimental rip currents. Figures 24–27 show the growth rates and dispersion relations for the sinuous modes of rip current instability at three different locations along the jet axis. It is immediately evident from these figures that the non-parallel effects strongly affect the growth rates and phase speeds of the disturbances and the growth rates decline as the jet spreads. In addition, the predicted dimensional timescales of the fastest growing modes compare well with the measured spectra shown in § 2.2. The predicted dimensional scales of the FGM for each test are listed in table 4 along with the measured values of the nearest significant spectral peak shown in figures 6, 7, and 8–10. It is evident that the predicted frequencies of the FGM do correspond with peaks in the measured spectra for tests C, D, and G. The predicted frequency agrees less well with that measured frequency in tests B and E.

Finally, it should be considered that the modelled mean velocity profiles used in the instability analysis were fit to measured data that includes the effects of the finite

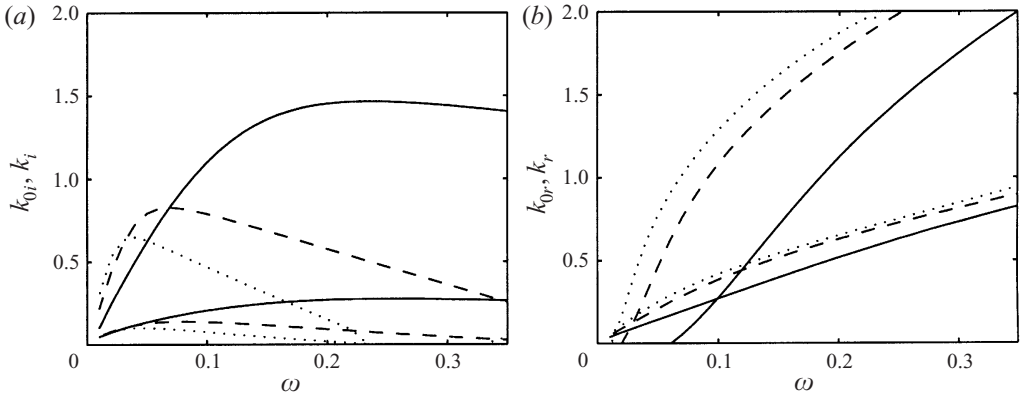


FIGURE 26. (*a*) Growth rate *vs.* frequency, (*b*) wavenumber *vs.* frequency for test E, all variables are non-dimensional. —, $x' = 0$ m; - - -, $x' = 0.3$ m; $\cdots$, $x' = 0.5$ m, upper curves include non-parallel effects ($k$), lower curves are for parallel flow theory ($k_0$).

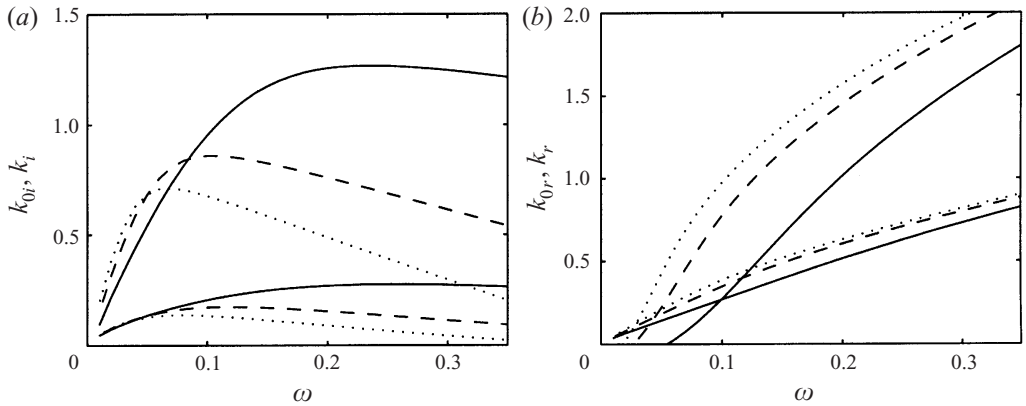


FIGURE 27. (*a*) Growth rate *vs.* frequency, (*b*) wavenumber *vs.* frequency for test G, all variables are non-dimensional. —, $x' = 0$ m; - - -, $x' = 0.3$ m; $\cdots$, $x' = 0.5$ m, upper curves include non-parallel effects ($k$), lower curves are for parallel flow theory ($k_0$).

| Test | $f_{FGM}$ (Hz) | $L_{FGM}$ (m) | $f_m$ (Hz) | $L_m$ (m) |
|---|---|---|---|---|
| B | 0.010 | 5.1 | 0.005 | — |
| C | 0.017 | 4.7 | 0.018 | 2.7 |
| D* | 0.032 | 6.1 | 0.033 | — |
| E | 0.020 | 2.5 | 0.01 | — |
| G | 0.013 | 3.5 | 0.013 | 2.0 |

TABLE 4. Table of predicted dimensional time and lengthscales of the FGM ($f_{FGM}, L_{FGM}$) at $x'$=0 m including non-parallel effects and the measured values of the nearest spectral peak estimated in §2.2. *Test D ($f_{FGM}, L_{FGM}$) includes parallel effects only.

disturbances. Therefore, the mixing induced by the disturbances will probably decrease the shear in the measured profile and reduce the growth rates in the corresponding linear stability analysis. This effect was considered directly in the nonlinear analysis of longshore current instabilities by Slinn *et al.* (1998). Their results indicated that

while the linear growth rates obtained from the measured profile (as opposed to the profile in the absence of disturbances) are decreased, the frequency and wavenumber scales of the disturbances are still well predicted by the linear stability analysis.

## 4. Summary

Rip currents have been generated in the laboratory on a barred beach with periodically spaced rip channels. The incident waves were monochromatic and normally incident to the shore; however, the wave height, wave period, and still water level were varied from test to test. The experiments consistently demonstrated the presence of low-frequency rip current oscillations in the presence of steady wave forcing. It is hypothesized that the sources of these rip oscillations are instabilities commonly found in shallow water jets.

Energy spectra measured near the rip neck show distinct low-frequency peaks. A limited analysis of cross-spectra show that the rip oscillations are offshore propagating wavelike motions. The presence of multiple spectral peaks in some tests suggests the presence of multiple unstable modes; alternatively, the presence of energies at sum frequencies may indicate that individual modes are interacting nonlinearly.

An analytical model for the mean flows in rip currents was developed in order to analyse the stability characteristics of rip currents. The model is based on the governing vorticity balance within offshore directed flows over variable (longshore uniform) topographies. The model includes the effects of a variable cross-shore beach profile, turbulent mixing, and bottom friction. The model uses a multiple scales technique and is strictly valid for long narrow jet-like currents. The mean rip current profiles are self-similar and related to the well-known Bickley jet solution.

The rip current scales $U_0, b_0, R_t, f_t$ are found by fitting the model velocity profiles to the measured data. The modelled profiles provide a good fit to the data and the non-dimensional mixing ($R_t$) and bottom friction parameters ($f_t$) determined from the fitting procedure suggest that turbulent mixing and bottom friction play a large role in the spreading of the rip current and the decay of the centreline velocity.

A linear stability model governing spatially growing rip current instabilities was developed which applies the non-parallel flow effects as a correction to the parallel flow problem. Our results indicate that non-parallel effects (turbulent mixing, bottom friction, and bottom slope) significantly increase the growth rates of the instabilities and decrease their phase speeds. In addition, the sinuous modes exhibit the fastest growth rates and the results for spatial instabilities are shown to differ significantly from the temporal instability results.

Finally, the predicted time and lengthscales of the fastest growing (linear) modes for each test are compared to the measured scales (when available). Though the measured instabilities appear to exhibit nonlinearity, the data do indicate the presence of energetic motions at frequencies near those predicted by the linear model. The model/data agreement for tests C, D, and G is well within the range of experimental uncertainty, the data from tests B and E are predicted less well. The results strongly suggest that a rip current instability mechanism can explain much of the low-frequency motions observed during the experiments.

As a final note, recently reported field measurements of rip current velocities by Aagaard, Greenwood & Nielsen (1997) suggest that rip instabilities may play a role in the transport of nearshore sediments. They describe low-frequency rip pulses as being an efficient mechanism for resuspending sediment from the bed. Though these authors attribute the low-frequency motion to the presence of low-frequency-gravity

waves, they also note that the low-frequency motions disappear when the rip flow ceases during the peak of the tidal cycle, even though the offshore wave conditions remain constant. This correlation of low-frequency energy in the rip with strong rip velocities suggests that rip instabilities are a possible alternative explanation for low-frequency rip oscillations.

This work was sponsored by the Office of Naval Research Coastal Dynamics Program grant N00014-95-1-0075 and grant N00014-98-1-0521. The authors also wish to thank Ib Svendsen for his contributions to the experimental project and for helpful comments on portions of this manuscript.

## Appendix A. Wave basin seiching

In this section we will investigate wave basin seiching as a potential source for low-frequency energy during the experiments. Wave generation in an enclosed basin will cause basin seiching owing to wave reflections or wave grouping effects that can transfer wave energy to low-frequencies. It is important, therefore, to quantify any influence of seiching on these experiments, especially in regard to the interpretation of the low-frequency rip current fluctuations.

In order to determine a solution for the basin seiche modes, we begin with the two-dimensional shallow-water wave equation for variable depth given by

$$\eta_{tt} - (gh\eta_x)_x - (gh\eta_y)_y = 0, \tag{A 1}$$

where $\eta$ is water surface elevation, $h$ is water depth, and subscripts represent derivatives. We will assume that the seiche modes are periodic in the longshore direction and in time, and have some arbitrary distribution in the cross-shore direction such that $\eta$ can be expressed as

$$\eta(x, y, t) = \zeta_m(x) \cos\left(\frac{n\pi y}{W}\right) \cos(\omega t), \tag{A 2}$$

where $\zeta_m$ is the eigenvector representing the cross-shore waveform, $n$ is the longshore mode number, $W$ is the width of the basin, and $\omega$ is the wave frequency. Substituting (A 2) into (A 1) and assuming a longshore uniform bathymetry ($h_y = 0$) we obtain the following governing equation for the seiche modes:

$$-gh\zeta_{m_{xx}} - gh_x\zeta_{m_x} + \frac{gh n^2\pi^2}{W^2}\zeta_m = \omega^2\zeta_m. \tag{A 3}$$

The boundary conditions for this problem are an impermeable wall at the wavemaker and finite wave amplitude at the shoreline. In order to implement the shoreline boundary condition it is convenient to make the following variable transformation $\xi = \zeta_m x$ and to orient the coordinate axis such that the still water shoreline is at $x = 0$ and the wavemaker is at $x = L$. The transformed governing equation now can be written as

$$-gh\xi_{xx} + \left(\frac{2gh}{x} - gh_x\right)\xi_x + \left(\frac{gh_x}{x} - \frac{2gh}{x^2} + \frac{gh n^2\pi^2}{W^2}\right)\xi = \omega^2\xi. \tag{A 4}$$

with boundary conditions

$$\left.\begin{array}{ll} \xi = 0, & x = 0, \\ \zeta_x = \xi_x/x - \xi/x^2 = 0, & x = L. \end{array}\right\} \tag{A 5}$$

| Tests C–F $h_0 = 70.36$ cm | | Test B $h_0 = 72.42$ cm | | Test G $h_0 = 74.41$ cm | | |
|---|---|---|---|---|---|---|
| $T$ (s) | $T^{-1}$ (Hz) | $T$ (s) | $T^{-1}$ (Hz) | $T$ (s) | $T^{-1}$ (Hz) | $n,m$ |
| 27.8 | 0.036 | 27.4 | 0.036 | 27.2 | 0.037 | 1,0 |
| 22.9 | 0.044 | 22.7 | 0.044 | 22.6 | 0.044 | 0,1 |
| 19.7 | 0.051 | 19.2 | 0.052 | 18.9 | 0.053 | 2,0 |
| 16.4 | 0.061 | 16.1 | 0.062 | 16.0 | 0.063 | 1,1 |
| 16.0 | 0.063 | 15.5 | 0.065 | 15.3 | 0.065 | 3,0 |

TABLE 5. The first five (largest period) seiche modes for each water level, $n$ is the number of longshore zero crossings, $m$ is the number of cross-shore zero crossings.

Equation (A 4) is an eigenvalue problem for which non-trivial solutions ($\xi$) exist for only certain eigenvalues ($\omega^2$). To solve this eigenvalue problem, we use a finite-difference method. The cross-shore depth profiles measured over the centre bar section were discretized and (A 4) was written in matrix form using central differences ($O(\Delta x^2)$). The eigenvalues and eigenvectors are then solved for each longshore mode using a matrix eigenvalue solver. Table 5 lists the periods and mode numbers of the first five seiche modes for the three different water levels used in the experiments.

## Appendix B. Determination of constants and similarity profile

The constants $C$ and $C_1$ are not independent and can be related by using the $x_1$-momentum equation,

$$UU_{x_1} + VU_y = [U_m^2 g(\eta)] - f_t \frac{U^2}{h}, \tag{B 1}$$

which, if integrated across the jet and applying the boundary conditions

$$\left.\begin{aligned} U(x_1, \pm\infty) &= 0, \\ g(x_1, \pm\infty) &= 0, \end{aligned}\right\} \tag{B 2}$$

gives us the governing equation for the axial jet momentum flux,

$$(hU_m^2 b)_{x_1} = -f_t {U_m}^2 b. \tag{B 3}$$

This equation shows that the axial jet momentum decays owing to the retarding effect of bottom friction. This is in contrast to the classical jet solution (flat bottom, $f_t = 0$), which conserves jet momentum flux in the axial direction. Substituting (3.25) and (3.26) into (B 3) and rearranging, yields the following relation

$$\frac{C}{C_1} = -2, \tag{B 4}$$

and evaluating 3.28 at $x_1 = 0$ yields $C_3 = 1$. Finally, we are left evaluating either $C$ or $C_1$ experimentally. We do this by evaluating (3.26) at $x_1 = 0$ (where $h = h_0 = 1$). This gives the following relation

$$C = -2(U_{m_{x_1}}(0) + f_t), \tag{B 5}$$

which can be evaluated using the fit to the measured data.

We have not yet specified $f(\eta)$ and $g(\eta)$. We can relate these two functions by

returning to (3.23) and substituting $\ell = b$ and $U_y = U_m f_\eta / b$ to obtain

$$g = \frac{f_\eta}{R_t}. \tag{B 6}$$

Substituting the above relation into (3.24) gives us the general equation for $f$ as

$$f_{3\eta} + \tfrac{3}{2} R_t C f f_\eta + \tfrac{1}{2} C R_t f_{\eta\eta} \int_0^\eta f \, \mathrm{d}\eta' = 0. \tag{B 7}$$

It can be verified by direct substitution that the solution to (B 7), subject to the boundary conditions $f(0) = 1$ and $f_\eta(0) = 0$, is

$$f = \operatorname{sech}^2 \left( \frac{\sqrt{C R_t}}{2} \eta \right). \tag{B 8}$$

As the last consideration, we formally define the width scale $b(x_1)$ in relation to the velocity profile as

$$\frac{U(x_1, b)}{U_m(x_1)} = \operatorname{sech}^2(1) \approx 0.42, \tag{B 9}$$

so that $b$ is defined as the distance from the jet axis where the axial velocity equals approximately 42% of the centreline velocity. By combining (B 8) and (B 9), we can relate the turbulent Reynolds number to the experimental parameter $C$

$$R_t = \frac{4}{C}, \tag{B 10}$$

and the similarity function can be written simply as $f = \operatorname{sech}^2 \eta$.

## Appendix C. Details of the linear instability solution

$$\mathscr{L}(\phi_1) = D, \tag{C 1}$$

where the coefficients are defined as

$$\left.\begin{aligned}
d_1 &= 2\mathrm{i}\omega - 3\mathrm{i}k_0 U - \mathrm{i}\frac{U_{yy}}{k_0}, \\
d_2 &= \frac{\mathrm{i}U}{k_0} \\
d_3 &= -\mathrm{i}k_0 V - \frac{\mathrm{i}V_{yy}}{k_0} - \frac{2\mathrm{i}h_{x_1}}{k_0 h} U_y + \frac{2\mathrm{i}f_t}{k_0 h} U_y, \\
d_4 &= \frac{iV}{k_0} \\
d_5 &= k_{0_{x_1}} \left( \frac{\mathrm{i}\omega}{k_0} - 3\mathrm{i}U \right) + \frac{h_{x_1}}{h}(-\mathrm{i}\omega + 3\mathrm{i}k_0 U) - f_t \frac{\mathrm{i}k_0 U}{h}, \\
d_6 &= -\frac{2\mathrm{i}h_{x_1}}{k_0 h} U - \frac{\mathrm{i}k_0 U_m b}{R_t} + 2\mathrm{i}\frac{f_t U}{k_0 h}, \\
d_7 &= -\frac{\mathrm{i}U_m b}{k_0 R_t}.
\end{aligned}\right\} \tag{C 2}$$

The solvability condition for (3.39) can be written as

$$\int_{-\infty}^{\infty} \mathscr{L}(\phi_1) \zeta^* \, \mathrm{d}y = 0, \tag{C 3}$$

where we have substituted the following expression for the eigenfunction

$$\phi_0 = A(x_1)\zeta(y; x_1), \tag{C 4}$$

where $A(x_1)$ is the amplitude of the disturbance and varies in the axial direction. Direct substitution for $D$ from (C 2) into (C 3) gives

$$\int_{-\infty}^{\infty} [d_1(A_{x_1}\zeta + A\zeta_{x_1}) + d_2(A_{x_1}\zeta_{yy} + A\zeta_{x_1yy}) + d_3A\zeta_y + d_4A\zeta_{yyy}]\ \phi_0^* + \int_{-\infty}^{\infty} [d_5A\zeta + d_6A\zeta_{yy} + d_7A\zeta_{yyyy}]\ \phi_0^* = 0, \tag{C 5}$$

and this can be rearranged to obtain the following evolution equation for $A(x_1)$,

$$A_{x_1} = \mathrm{i}k_1(x_1)A \tag{C 6}$$

where

$$k_1 = \frac{\mathrm{i}\displaystyle\int_{-\infty}^{\infty} (d_1\zeta_{x_1} + d_2\zeta_{x_1yy} + d_3\zeta_y + d_4\zeta_{3y} + d_5\zeta + d_6\zeta_{yy} + d_7\zeta_{4y})\phi_0^*\,\mathrm{d}y}{\displaystyle\int_{-\infty}^{\infty} (d_1\zeta_{+}d_2\zeta_{yy})\phi_0^*\,\mathrm{d}y}, \tag{C 7}$$

and the terms $d_1$ to $d_7$ are defined by (C 2).

### C.1. *Numerical method*

The boundary conditions for the eigenvalue problem described by (3.38) are as follows:

$$\phi_0 = \phi_{0_y} \to 0 \quad \text{as} \quad y \to \pm\infty, \tag{C 8}$$

$$\begin{aligned} \phi_{0_y} = 0 \quad &\text{at} \quad y = 0 \to \text{sinuous mode}, \\ \phi_0 = 0 \quad &\text{at} \quad y = 0 \to \text{varicose mode}. \end{aligned} \tag{C 9}$$

In order to implement the boundary condition (C 8) at a finite value of $y$, we use the conditions $U, U_{yy} \to 0$ as $y \to \infty$ to obtain the asymptotic form of (3.38). Given an $\omega$ and an initial guess for $k_0$, the solution ($\phi_0 = \exp(-k_0y)$) to the asymptotic equation is applied at a sufficiently large $y$ and then (3.38) is integrated (shooting method) using a fourth-order Runge–Kutta algorithm (Hoffman 1992). At $y = 0$, the boundary condition (C 9) is evaluated, and $k_0$ is iterated using the secant method until the wavenumber is found which satisfies the boundary condition.

With $k_0$ known, (3.42) is integrated using a similar procedure; however, only one iteration is necessary since the adjoint problem has the same eigenvalues as the original problem. The calculation of $\phi_0^*$ can then be used as a check on the accuracy of the computed eigenvalues. Equation (3.40) is also integrated using a similar procedure. The step size for the numerical integration procedure was generally $\Delta y = 0.0005b(x_1)$, and, therefore, varied in the axial direction. The distance from the jet axis where (C 8) was implemented was $y = 6b(x_1)$.

## REFERENCES

Aagaard, T., Greenwood, B. & Nielsen, J. 1997 Mean currents and sediment transport in a rip channel. *Mar. Geol.* **140**, 25–45.

Arthur, R. S. 1950 Refraction of shallow water waves: the combined effect of currents and underwater topography. In *Eos Trans. AGU*, **31**, 4, 549–551.

Arthur, R. S. 1962 A note on the dynamics of rip currents. *J. Geophys. Res.* **67**, 2777–2779.

Bickley, W. 1939 The plane jet. *Phil. Mag. Ser.* **7**, 727–731.

Bowen A. J. 1969 Rip currents, 1. Theoretical investigations. *J. Geophys. Res.* **74**, 5467–5478.

Bowman, D., Arad, D., Rosen, D. S., Kit, E., Goldbery, R. & Slavicz A. 1988 Flow characteristics along the rip current system under low-energy conditions. *Mar. Geol.* **82**, 149–167.

Dalrymple, R. A. 1975 A mechanism for rip current generation on an open coast. *J. Geophys. Res.* **80**, 3485–3487.

Dalrymple, R. A. & Lozano, C. J. 1978 Wave–current interaction models for rip currents. *J. Geophys. Res.* **83**, C12, 6063–6071.

Dodd, N. & Falqués A. 1996 A note on spatial modes in longshore current shear instabilities. *J. Geophys. Res.* **101**, C10, 22 715–22 726.

Drazin, P. G. & Howard L. N. 1966 Hydrodynamic stability of parallel flow of inviscid fluid. In *Advances in Applied Mechanics* (ed. G. Kuerti), vol. 7, pp. 1–89. Academic.

Falqués, A. & Iranzo V. 1994 Numerical simulation of vorticity waves in the nearshore. *J. Geophys. Res.* **99**, C1, 825–841.

Garg, V. K. & Round G. F. 1978 Nonparallel effects on the stability of jet flows. *J. Appl. Mech.* **45**, 717–722.

Gaster, M. 1962 A note on the relation between temporally-increasing and spatially-increasing disturbances in hydrodynamic stability. *J. Fluid Mech.* **14**, 222–224.

Greenberg, M. D. 1988 *Advanced Engineering Mathematics*. Prentice–Hall.

Haller, M. C. & Dalrymple R. A. 1999 Rip current dynamics and nearshore circulation. *Res. Rep. CACR-99-05* (also PhD thesis), Center for Applied Coastal Research, University of Delaware, Newark.

Haller, M. C., Dalrymple, R. A. & Svendsen I. A. 2000 Experiments on rip currents and nearshore circulation: data report. *Res. Rep. CACR-00-04*, Center for Applied Coastal Research, University of Delaware, Newark.

Hoffman, J. D. 1992 *Numerical Methods for Engineers and Scientists*. McGraw–Hill.

Huntley, D. A. & Short, A. D. 1992 On the spacing between observed rip currents. *Coastal Engng* **17**, 211–225.

Iwata, N. 1976 Rip current spacing. *J. Ocean. Soc. Japan* **32**, 1–10.

Joshi, P.B. 1982 Hydromechanics of tidal jets. *J. Waterways, Port, Coast. Ocean Engng* **108**, WW3, 239–253.

Kobayashi, N., Karjadi, E. A. & Johnson, B. D. 1997 Dispersion effects on longshore currents in surf zones. *J. Waterways, Port, Coast. Ocean Engng* **123**, 240–248.

Mei, C. C. 1989 *The Applied Dynamics of Ocean Surface Waves*. World Science, River Edge, NJ.

Nayfeh, A. H., Saric, W. S. & Mook, D. T. 1974 Stability of non-parallel flows. *Arch. Mech.* **26**, 401–406.

Schlichting, H. 1933 *Laminare Strahlenausbreitung, Z. Angew. Math. Mech.* **13**, 260–263.

Shepard, F. P., Emery, K. O. & La Fond, E. C. 1941 Rip currents: a process of geological importance. *J. Geol.* **49**, 337–369.

Slinn, D. N., Allen, J. S., Newburger, P. A. & Holman R. A. 1998 Nonlinear shear instabilities of alongshore currents over barred beaches. *J. Geophys. Res.* **103**, 18 357–18 379.

Smith, J. A. & Largier, J. L. 1995 Observations of nearshore circulation: rip currents. *J. Geophys. Res.* **100**, 10 967–10 975.

Sonu, C. J. 1972 Field observation of nearshore circulation and meandering currents. *J. Geophys. Res.* **77**, 3232–3247.

Tam, C. K. W. 1973 Dynamics of rip currents. *J. Geophys. Res.* **78**, 1937–1943.

Tennekes, H. & Lumley, J. L. 1972 *A First Course in Turbulence*. MIT Press.

Wilmott, C. J. 1981 On the validation of models. *J. Phys. Oceanogr.* **2**, 219–232.

Yoon, S. B. & Liu P. L.-F. 1990 Effects of opposing waves on momentum jets. *J. Waterways, Port, Coast. Ocean Engng* **116**, 545–557.